



# MiM: Mask in Mask Self-Supervised Pre-Training for 3D Medical Image Analysis

Jia-Xin Zhuang<sup>a</sup>, Linshan Wu<sup>a</sup>, Qiong Wang<sup>e</sup>, Varut Vardhanabhuti<sup>f</sup>, Lin Luo<sup>g</sup>, Hao Chen<sup>a,b,c,d,\*</sup>

<sup>a</sup>Department of Computer Science and Engineering, Hong Kong University of Science and Technology, Hong Kong SAR, China

<sup>b</sup>Department of Chemical and Biological Engineering, Hong Kong University of Science and Technology, Hong Kong SAR, China

<sup>c</sup>Division of Life Science, Hong Kong University of Science and Technology, Hong Kong SAR, China

<sup>d</sup>HKUST Shenzhen-Hong Kong Collaborative Innovation Research Institute, Futian, Shenzhen, China

<sup>e</sup>Shenzhen Institutes of Advanced Technology, Chinese Academy of Sciences, Shenzhen, China

<sup>f</sup>Department of Diagnostic Radiology, The University of Hong Kong, Hong Kong SAR, China

<sup>g</sup>College of Engineering, Peking University, Beijing, China

## ARTICLE INFO

### Article history:

Received 1 May 2013

Received in final form 10 May 2013

Accepted 13 May 2013

Available online 15 May 2013

Communicated by S. Sarkar

**Keywords:** CT, Self-Supervised Learning, Segmentation, Classification, 3D medical images.

## ABSTRACT

The Vision Transformer (ViT) has demonstrated remarkable performance in Self-Supervised Learning (SSL) for 3D medical image analysis. Mask AutoEncoder (MAE) for feature pre-training can further unleash the potential of ViT on various medical vision tasks. However, due to large spatial sizes with much higher dimensions of 3D medical images, the lack of hierarchical design for MAE may hinder the performance of downstream tasks. In this paper, we propose a novel *Mask in Mask (MiM)* pre-training framework for 3D medical images, which aims to advance MAE by learning discriminative representation from hierarchical visual tokens across varying scales. We introduce multiple levels of granularity for masked inputs from the volume, which are then reconstructed simultaneously ranging at both fine and coarse levels. Additionally, a cross-level alignment mechanism is applied to adjacent level volumes to enforce anatomical similarity hierarchically. Furthermore, we adopt a hybrid backbone to enhance the hierarchical representation learning efficiently during the pre-training. MiM was pre-trained on a large scale of available 3D volumetric images, *i.e.*, Computed Tomography (CT) images containing various body parts. Extensive experiments on thirteen public datasets demonstrate the superiority of MiM over other SSL methods in organ/lesion/tumor segmentation and disease classification. We further scale up the MiM to large pre-training datasets with more than 10k volumes, showing that large-scale pre-training can further enhance the performance of downstream tasks. The improvement also concluded that the research community should pay more attention to the scale of the pre-training dataset towards the healthcare foundation model for 3D medical images.

© 2024 Elsevier B. V. All rights reserved.

## 1. Introduction

Deep learning has made significant progress in medical image analysis, albeit limited to the supervised learning paradigm that relies on a relatively large amount of labeled training

data (Shen et al., 2017; Zhuang et al., 2023a). However, labeling 3D medical images is a time-consuming and labor-intensive process that requires expertise (Jin et al., 2023; Tajbakhsh et al., 2020). Specifically, to expand the training set while reducing human intervention, Semi-supervised Learning and Self-Supervised Learning (SSL) has been become a promising direction (Chen et al., 2023b; He et al., 2022, 2020; Chen

\*Corresponding author (Email: [jhc@cse.ust.hk](mailto:jhc@cse.ust.hk))

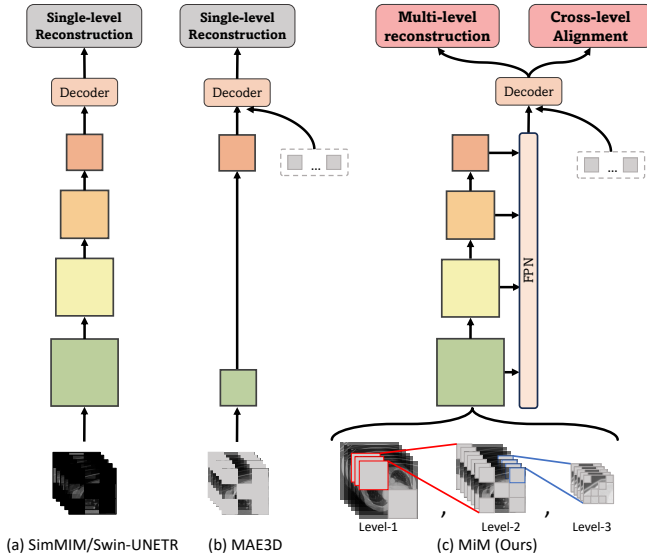


**Fig. 1. Different SSL for 3D medical image analysis.** Current Masked Image Modeling methods for 3D medical images primarily (a) rely on pretext tasks *e.g.*, inpainting, at a *single level*, utilizing hybrid transformers to incorporate all tokens or (b) employ an MAE that reconstructs at a *single level* using visible tokens. In contrast, (c) we observe that 3D medical images inherently exhibit hierarchical properties. Thus, our Mask in Mask (MiM) framework aims to encode *multi-level* 3D medical image learning across hierarchical visual tokens at various scales through *multi-level reconstruction* and *cross-level alignment* (we set the number of level  $L$  to 3 in this figure). Additionally, our framework employs a hybrid transformer while only using visible tokens.

*et al.*, 2020a; Wu *et al.*, 2023b). Among them, SSL has shown great potential in learning transferable representations from unlabeled data without any annotations, which can be further fine-tuned on downstream tasks to enhance the task performance (Jiang *et al.*, 2023; He *et al.*, 2023; Tang *et al.*, 2022; Xie *et al.*, 2022a; Wang *et al.*, 2023d; Zhou *et al.*, 2021c, 2023; Zhuang *et al.*, 2023b).

MAE-based methods (He *et al.*, 2022; Chen *et al.*, 2023a; Tong *et al.*, 2022; Feng and Zhang, 2023; Wang *et al.*, 2023a,b; Liu *et al.*, 2023a; Xie *et al.*, 2022b) has achieved high performance in various natural image analysis tasks by learning transferable representations through reconstructing the original output in pixels from its highly-masked version based on the ViT structure. However, 3D medical images such as Computed Tomography (CT), which are often volumetric and in a much higher dimension, contain a multi-granularity of visual details. Existing methods (Jiang *et al.*, 2023; He *et al.*, 2023; Tang *et al.*, 2022; Xie *et al.*, 2022a; Wang *et al.*, 2023d; Zhou *et al.*, 2021c, 2023; Zhuang *et al.*, 2023b; Xiao *et al.*, 2023; Wang *et al.*, 2024; Wolf *et al.*, 2023) like Swin-UNETR (Tang *et al.*, 2022) proposes to learn local and global representation by combining tailored proxy tasks including inpainting, rotation, and contrastive different views. He *et al.* (2023) further explores the geometric similarity between global and local crops by affirmation and matching. Jiang *et al.* (2023), on the other hand, maximizes the similarity between different views that contain consistent semantics. MAE3D (Chen *et al.*, 2023b) reconstructs the missing pixel based on a cropped volume. These methods mainly focus on encoding the 3D medical image from local or global

perspectives at a single scale, which may still result in the loss of finer granularity detail.

In the case of medical images in large spatial sizes of high dimensions, the use of hierarchical design is crucial for effective analysis and interpretation of clinical information (Chen *et al.*, 2022; Tang *et al.*, 2022; He *et al.*, 2023; Hosseinzadeh Taher *et al.*, 2023). In this paper, we propose a novel framework that enhances representation learning of MAE for 3D medical images by hierarchical design, as illustrated in Fig. 1. To achieve this goal, our framework utilizes a hierarchical view of 3D medical images, containing rich multi-granularity of clinical information essential for further analysis and providing important clinical insights. To obtain hierarchical masked volumetric inputs, we propose a multi-level volume generation strategy. This strategy conveys information from a coarse to a finer level, which combines to bring forth a rich representation of the model. We employ multi-level reconstruction to simultaneously reconstruct the masked volumes with multi-granularity details to learn discriminative representation. Compared to single-level reconstruction (Chen *et al.*, 2023b; Wang *et al.*, 2023a; Xie *et al.*, 2022b; Gao *et al.*, 2022a), multi-level reconstruction can capture more detailed information and improve representation learning (Wang *et al.*, 2023b). Our multi-levels are constructed by dividing the original volume into multiple levels, which is different from the multi-scale strategy that uses different scales of the same volume (Wang *et al.*, 2023b; Hosseinzadeh Taher *et al.*, 2023). Cross-level alignment between adjacent level volumes is applied to learn both the global context information and local details, achieving better representation. Positive pairs *i.e.*, volumes from the same original volumes but at the adjacent level granularity, share the same clinical information. We enable the model to learn more robust representations by aligning the features of these volumes at different scales. We extend the hybrid backbone for MAE (Gao *et al.*, 2022a) from 2D natural images to our 3D medical image pre-training framework to further improve the efficiency during the pre-training period. Since previous MAE-based works (Xie *et al.*, 2022b) require all tokens to be kept in the later transformer stages, leading to an unaffordable computation cost. This leads to the loss of MAE’s efficiency advantage.

In summary, our contribution can be categorized into three aspects:

1. We propose a simple yet effective SSL framework, called MiM, which advances MAE with hierarchical design in 3D medical image pre-training, pushing the representability of pre-trained models.
2. MiM encodes multi-level visual cues across various scales into the metric, providing a reliable measurement of the hierarchical structure of 3D medical images. A multi-level volume generation strategy is proposed, and two tailored proxy tasks, multi-level reconstruction, and cross-level alignment, are presented, which simultaneously learn powerful local and global representations.
3. We pre-train MiM with various sizes of pre-training datasets ranging from  $1k$  to  $10k$  volumes. Extensive experiments demonstrate its effectiveness and achieve state-of-the-art performance across various tasks on thirteen pub-

lic datasets. We conclude that scaling up the pre-training dataset can further improve the performance of MiM.

## 2. Related works

In this section, we first review the previous mainstream self-supervised learning paradigms, especially for existing SSL methods for 3D medical images. Then we introduce the recent advances in masked image modeling and hierarchical design of SSL for 3D medical images for comparison with our method and highlight the differences.

**SSL for Medical Image Analysis.** Previous studies in SSL can be categorized into two primary paradigms: Contrastive learning and Pretext task (He et al., 2020; Chen et al., 2020a; Gao et al., 2022b). *Contrastive learning* methods bring positive pairs of images (*e.g.*, different views of the same image) closer and separate negative pairs (*e.g.*, different images) away in the feature space (Chen et al., 2020b,a; He et al., 2020; Chen et al., 2020c, 2021c). For example, MoCo v3 utilized a memory bank to maintain consistent representations of negative samples during contrastive learning (He et al., 2020; Chen et al., 2021b,c). These works have also shown effectiveness in medical image analysis, such as dermatology classification and chest X-ray classification (Zhao and Yang, 2021; Zhou et al., 2021b; Ye et al., 2022). However, previous contrastive learning approaches have primarily focused on the semantic misalignment of different instances, leading to minor improvements in dense prediction, such as segmentation (Chaitanya et al., 2020; Wu et al., 2024; Zhang et al., 2022b; Zhou et al., 2021b). *Pretext task*, on the other hand, are designed to explore the inner space structure information of images and have shown promise in dense prediction tasks (Chen et al., 2019; Haghghi et al., 2022; Tao et al., 2020; Xie et al., 2020). For example, Zhou et al. (2021c) proposed to directly pre-train a CNN model by restoring volumetric medical images from their distorted versions. Zhu et al. (2020) utilized the concept of solving a Rubik’s Cube to learn structural features from the volumetric medical data. Additionally, five common pretext tasks have been verified to be effective for volumetric image pre-training (Taleb et al., 2020). Tang et al. (2022) proposed to pre-train a 3D swin transformer (Liu et al., 2021) with the combination of three pretext tasks. Recently, Masked Image Modeling (He et al., 2022; Xie et al., 2022b), considered as widely used pretext tasks based, shows its effectiveness on 3D medical analysis (Chen et al., 2023b; Xiao et al., 2023; Zhuang et al., 2023b).

**Masked Image Modeling.** Masked Image Modeling is a generative SSL technique that involves training on images that have been corrupted by masking (He et al., 2022; Xie et al., 2022b; Chen et al., 2023b,a; Wang et al., 2023a,d; Xiao et al., 2023; Wang et al., 2024; Zhuang et al., 2023b). Previous researches on this technique, such as Vincent et al. (2010) and Pathak et al. (2016), treated masking as a type of noise and used inpainting techniques to predict the missing pixels. Dosovitskiy et al. (2020) investigated masked patch prediction by predicting the mean color of images. He et al. (2022) adhered to the spirit of raw pixel restoration and demonstrated that masking a high proportion of input images can yield a non-trivial and meaningful self-supervisory task. Chen et al. (2023a); Wang et al.

(2023a) proposes to improve masking priority strategies (Wang et al., 2023a) and the reconstruction targets (Chen et al., 2023a). Zhang et al. (2023); Wang et al. (2024) introduce the concept of Masked Image Modeling to versatile 2D medical scenario *e.g.* disease classification (Xiao et al., 2023) and segmentation (Wang et al., 2024). Chen et al. (2023b) represented a recent advancement in Masked Image Modeling (He et al., 2022; Xie et al., 2022b) for 3D CT in medical image analysis. Zhuang et al. (2023b) proposed to advance MAE for 3D medical image analysis, from the global and local perspectives by incorporating the contrastive learning paradigm.

Our method follows the primary idea of Masked Image modeling. As shown in Fig. 1, to address the existing problems mentioned above, instead of single-level masking, MiM leverages the hierarchical design inherent in the 3D medical images to generate multi-level volume for reconstruction and cross-level alignment, which can effectively capture the hierarchical structure of 3D medical images and improve the representation learning.

**Hierarchical SSL.** Hierarchical SSL has been investigated in numerous studies (Xie et al., 2022b; Chen et al., 2023a; Gao et al., 2022a; Zhang et al., 2022a) in the context of natural images. Xie et al. (2022b) and Chen et al. (2023a) proposed to incorporate Masked Image Modeling (He et al., 2022) with a hierarchical backbone *e.g.*, Swin Transformer (Liu et al., 2021). Wang et al. (2023b) reconstructing masked patches on multi-scale features using ViT (Dosovitskiy et al., 2015), while Gao et al. (2022a) advocated for predicting masked patches using only visible patches and a hierarchical backbone. Hosseinzadeh Taher et al. (2023) divided single-scale images into multi granularities and aligned their contrastive views (He et al., 2020; Chen et al., 2020c) with ResNet (He et al., 2016).

However, the relatively low dimensionality of 2D images limits the effectiveness of learning the hierarchical structure of 3D medical images given a single-level image with hybrid features. Furthermore, previous methods (Hosseinzadeh Taher et al., 2023; Wang et al., 2023b) treated each level image separately, neglecting the cross-level shared semantics.

In this paper, we propose a novel pretext task of Masked Image Modeling with a hierarchical design tailored for 3D medical images. This approach considers the inherent hierarchical design of 3D medical images during pre-training. Distinct from previous methods, we introduced a totally different Masked Image Modeling paradigm for 3D medical images. Our proposed hierarchical Masked Image Modeling paradigm employs multi-level volume generation for reconstruction and cross-level alignment, effectively capturing the hierarchical structure of 3D medical images and enhancing representation learning.

## 3. Methodology

This section provides an overview of our proposed MiM method. Firstly, the overall framework of the MiM method is introduced in Section 3.1. Secondly, the process of multi-level reconstruction is presented in Section 3.2. Then, the cross-level alignment via contrastive learning in our proposed MiM method is described in Section 3.3. Finally, the backbone of the MiM method in the pre-training period is introduced in Section 3.4.

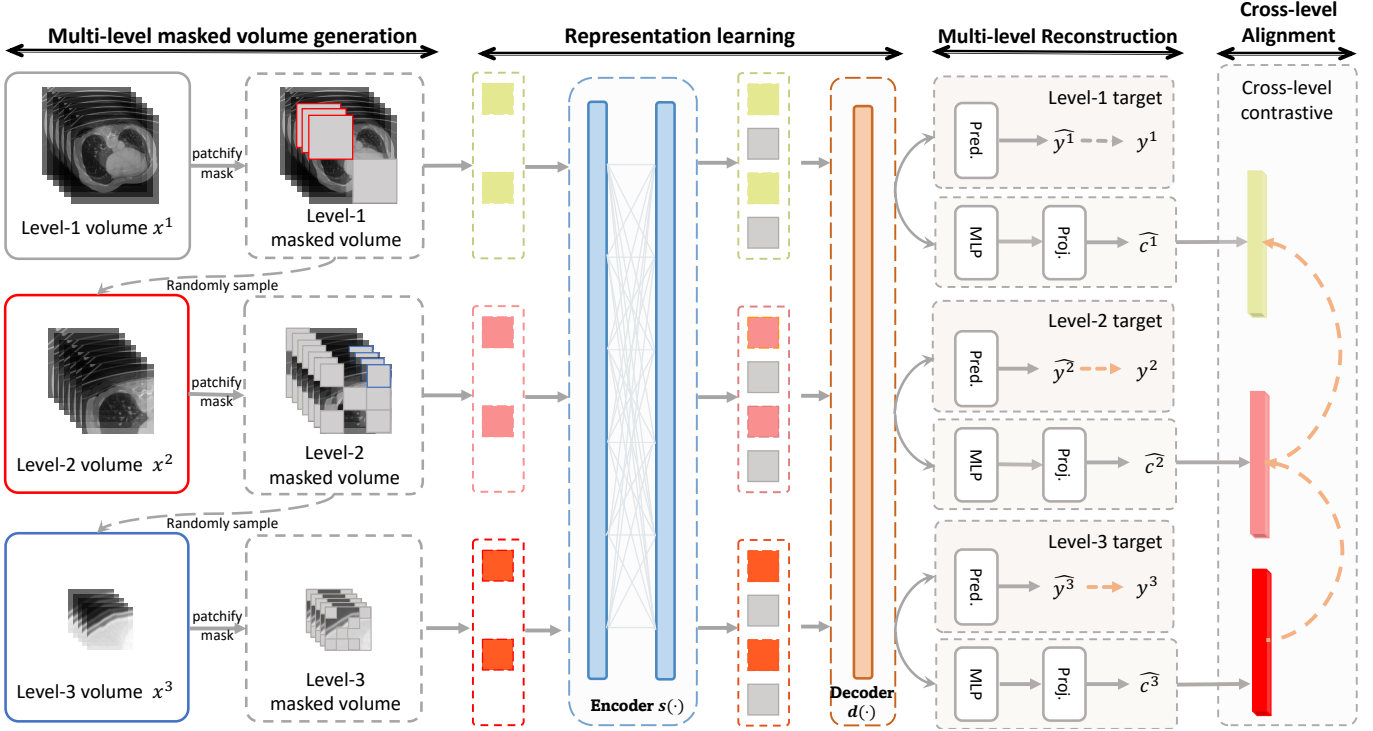


Fig. 2. The overall framework of our MiM pre-training framework. The level  $L$  is set to 3 for better illustration. We first conduct the process of multi-level masked volume generation. The multi-level reconstruction module is responsible for reconstructing the masked volumes at different levels. The cross-level alignment module aligns representations of volumes between volumes from adjacent levels, aiming to enforce anatomical similarity in a hierarchical manner.

### 3.1. Overall framework

The proposed MiM method’s overall framework is presented in Fig. 2, which comprises multi-level reconstruction modules and cross-level alignment modules. To pre-train the model with MiM, we first generate multi-level volumes from the input 3D medical images. Then, an input volume is cropped into non-overlapping patches, which are divided into unmasked patches and masked patches. The unmasked patches are transformed into a high-dimension feature space using a typical backbone (CNN (He et al., 2016) and transformer (Dosovitskiy et al., 2020)). The masked patches are used to generate the next level of masked volumes for multi-level learning. The goal is to restore the masked patches from different levels of masked volumes. In this paper, instead of a single level of masked volume (Feng and Zhang, 2023; Wang et al., 2023a,b), we propose to ease this goal by multi-level of masked volume. We developed a  $\mathcal{L}_R$  to supervise the final prediction. In addition, we further use a loss function  $\mathcal{L}_C$  to align the shared semantics between the cross-level volumes, aiming to learn the global semantic content as well as local details. Further details are presented in Section 3.2 and Section 3.3.

### 3.2. Multi-level reconstruction

**Generation of multi-level masked volumes.** Given a volumetric image  $x \in \mathbb{R}^{CHWD}$  (e.g.,  $C = 1$  for CT), we aim to generate multi-level volumes  $\{x^l \in \mathbb{R}^{CH^l W^l D^l}, l \in L\}$ , which contains  $L$  numbers of level, i.e., different granularity information from coarse to fine level. The generation of multi-level volume is illustrated in Fig. 3. We start by cropping a large portion of sub-volume from  $x$  as Level-1 volume  $x^1 \in \mathbb{R}^{CH^1 \times W^1 \times D^1}$ . The

level 1 volume  $x^1$  is then patchified into  $N$  non-overlapping visual tokens using a patch of  $\{\frac{H}{6}, \frac{W}{6}, \frac{D}{6}\}$  as in (He et al., 2022; Chen et al., 2023b; Zhuang et al., 2023b). Following previous MAE-based methods (Chen et al., 2023b; Zhuang et al., 2023b), we apply a high mask ratio  $\mu$  (e.g., 60%) to the  $N$  non-overlapping visual tokens (e.g., 216), resulting in visible tokens and invisible tokens. Each visible token is resized at spatial dimension to  $\mathbb{R}^{Chwd}$  before further processed by a linear project as previous MAE-based methods (Chen et al., 2023b; Zhuang et al., 2023b). The invisible tokens from Level-1  $x^1$  are considered as the next level volume, i.e., Level-2 volume  $x^2 \in \mathbb{R}^{CH^2 \times W^2 \times D^2}$ . It’s noted that the Level-2 volume  $x^2$  is generated from the *masked patches* of Level-1 volume  $x^1$ , instead of unmasked patches. The content of the target reconstruction at different levels shares regions, meaning that the volumes for Level-1 and Level-2 reconstruct overlapping regions but from different granularities, respectively. This can effectively capture the hierarchical structure of 3D medical images and improve representation learning Wang et al. (2023b). Ablation study of the reconstruction targets, i.e., the choices of masked patches or unmasked patches as next level volume, is presented in Section 4.7.1. Since there exist many invisible tokens, we randomly sample  $\gamma$  times without replacement from these tokens for computation efficiency.

The Level-2 volume  $x^2$  is also patchified into  $N$  non-overlapping visual tokens with a patch size of  $\{\frac{H_2}{6}, \frac{W_2}{6}, \frac{D_2}{6}\}$ . With applying the mask ratio  $\mu$  as in the previous process, the visible tokens from Level-2 volume  $x^2$  are resized to  $\mathbb{R}^{Chwd}$  before feeding the backbone. Meanwhile, the invisible tokens from Level-2 volume  $x^2$  are considered as next finer level vol-

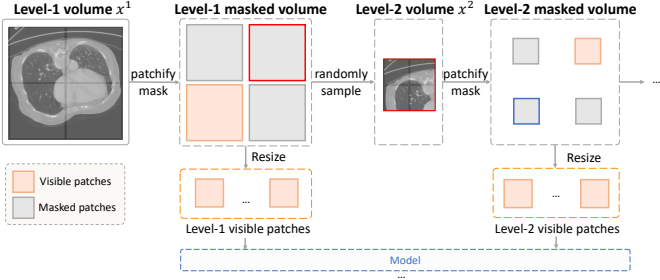


**Fig. 3. Illustration of the multi-level masked volume generation.** The level  $L$  is set to 2 and slices drawn from the 3D medical images are shown in the figure for better illustration. Level-2 volume  $x^2$  is randomly sampled from the *masked patches* of Level-1 volume  $x^1$  (*i.e.*, patch with red box). Consequently, the content of the target reconstruction at different levels shares regions, meaning that the volumes for Level-1 and Level-2 reconstruct overlapping regions but from different granularities, respectively.

ume *i.e.*, Level-3 volume  $x^3 \in \mathbb{R}^{CH^3 \times W^3 \times D^3}$ . Similarly, we randomly sample  $\beta$  times without replacement from these tokens for computation efficiency. This generation process of multi-level volume is repeated until the last level of volume  $x^L$  is generated.

Thus, all visible tokens from different levels are fed into the backbone to extract the high-dimension features  $z$ . Following previous SSL methods (He *et al.*, 2022; Chen *et al.*, 2023b; Zhuang *et al.*, 2023b), a lightweight decoder is used to project  $z$  along with learnable invisible tokens into latent features  $q$ . For reconstruction, the decoder followed by a simple prediction head is used to reconstruct the invisible tokens  $y$ . For cross-level alignment, all visual tokens from identical levels are aggregated by MLP layers and then projected into a context vector  $c$ .

**Single-level reconstruction.** Our reconstruction target is the pixel values of the invisible tokens for each level volume. With feature extracted from the backbone and the decoder with a prediction head (*i.e.*, a linear layer), following previous MAE methods (Chen *et al.*, 2023b; Zhuang *et al.*, 2023b), we reshape the prediction results and reconstruction targets to one-dimensional vector, *i.e.*,  $\hat{y} \in \mathbb{R}^{1 \times C}$  and  $y \in \mathbb{R}^{1 \times C}$ , where  $C$  is the number of dimensions. Specifically, we empirically set the  $C$  to 768, as in (He *et al.*, 2022; Chen *et al.*, 2023b; Zhuang *et al.*, 2023b).

Then we compute the differences  $d$  between the reconstruction target  $y$  and the prediction result  $\hat{y}$ . Specifically, we use MSE distance (He *et al.*, 2022; Chen *et al.*, 2023b) to measure the difference  $d_m$  between the prediction result and the reconstruction target for each masked token  $m$  as follows:

$$d_m = \|y_m - \hat{y}_m\|_2, m \in M, M = \mu N, \quad (1)$$

where  $M$  denotes the numbers of masked tokens and  $d_m$  ranges from 0 to 1. Lower  $d_m$  indicates the smaller difference between the prediction result  $\hat{y}_m$  and the reconstruction target  $y_m$ .

Aiming to minimize the difference  $d_m$ , we define the reconstruction loss  $\mathcal{L}_R^l$  for each level of masked volumetric images  $l \in L$  as follows:

$$\mathcal{L}_R^l = \frac{1}{|M|} \sum_{m=1}^{|M|} d_m^l, l \in L, \quad (2)$$

where  $M$  represents the number of mask tokens. The reconstruction loss is computed as the sum of squared differences between the reconstruction target and the reconstructed representations based on pixel values.

**Loss function for multi-level reconstruction.** To learn multi-granularity details from 3D volumetric images, We apply multi-level reconstruction for each level of masked volumetric images, ranging from coarser levels to finer levels. The formulation of the multi-level reconstruction loss  $\mathcal{L}_R$  is shown as follows:

$$\mathcal{L}_R = \frac{1}{L} \sum_{l=1}^L \mathcal{L}_R^l \quad (3)$$

### 3.3. Cross-level alignment

The alignment between the shared semantic patches of cross-level volumes from fine-to-coarse can enforce anatomical similarity in a hierarchical manner. Fig. 4 illustrates the process of cross-level alignment. Since we generate the finer level volumes from the coarser level volumes (*e.g.*, Level-2 volumes generated from masked patches of the Level-1 volumes), these volumes must share semantic context, which can be regarded as positive pairs. In contrast, the non-overlap patches in the coarser volumes (*e.g.*, the rest patches in the Level-1 volumes) are considered as negative patches. To enlarge the high-dimensional feature consistency for shared anatomical structure patches (*i.e.*, *positive pairs*) and discrepancy between non-overlap patches (*i.e.*, *negative pairs*), we apply contrastive learning (Chen *et al.*, 2020a) to the context vector  $c$  and patches  $p$ . Specially, we reshape the context vector and patches its coarser volumes to one-dimension vector  $c \in \mathbb{R}^{1 \times D}$  and  $\{p_i \in \mathbb{R}^{1 \times D}, i \in N\}$ , where  $D$  is the number of dimensions, empirically set  $D$  to 2048, as in (Caron *et al.*, 2021).

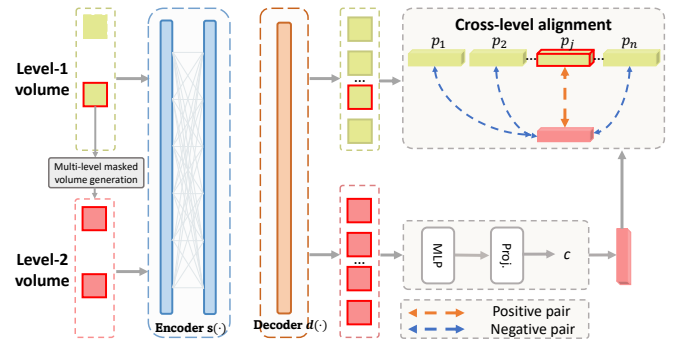


**Fig. 4. Illustration of cross-level alignment module.** We set level  $L$  to 2 for better illustration. The Level-2 context representation and the corresponding patches of Level-1 volumes are regarded as positive pairs. The rest patches of the Level-1 volume are considered negative pairs.

First, given the context vector  $c_i$  and the patches  $p$ , we compute the cosine similarity  $s_{ij}$  between the context vector  $c_i$  and the patches  $p_j$  as follows:

$$s_{ij} = \cos \text{Sim}(c_i, p_j) = \frac{c_i \cdot p_j}{\|c_i\| \|p_j\|}, i \in M, j \in N. \quad (4)$$

We aim to maximize the cosine similarity between the context vector  $c_i$  and the positive patches  $p$  and minimize the cosine similarity between the context vector  $c_i$  and the negative

patches  $p_j$  from the rest patches of the volumes. Thus, we apply the contrastive loss (Chen and He, 2020) to implement this goal as follows,

$$\ell_{ij} = -\log \frac{\exp(s_{ij}/\tau)}{\sum_{k=1}^N \mathbb{1}_{k \neq i} \exp(s_{ik}/\tau)}, i \in M, j \in N, M \in \mu N. \quad (5)$$

Thus, the cross-level alignment loss  $\mathcal{L}_C^{l,l+1}$  between adjacent level  $l$  and  $l+1$  volumes is computed as follows:

$$\mathcal{L}_C^{l,l+1} = \frac{1}{M \cdot N} \sum_{i=1}^M \sum_{j=1}^N \ell_{ij}, l \in L-1, M \in \mu N. \quad (6)$$

The cross-level alignment loss is computed as the sum of the negative log-likelihood of the cosine similarity between the context vector and the rest patches from the coarser volumes.

The formulation of cross-level alignment  $\mathcal{L}_C$  is defined as the average of the cross-level alignment loss between adjacent level volumes, as shown in Eq. 7,

$$\mathcal{L}_C = \frac{1}{L-1} \sum_{l=1}^{L-1} \mathcal{L}_C^{l,l+1} \quad (7)$$

By minimizing the overall cross-level alignment loss, we can enforce anatomical similarity hierarchically.

### 3.4. Backbone

Previous hybrid transformers, such as nnFormer (Zhou et al., 2021a) and Swin-UNETR (Hatamizadeh et al., 2021; Tang et al., 2022), aim to produce pyramid features. However, they suffer from complexity, needing to process all visual tokens for Masked Image Modeling, which is inefficient (Gao et al., 2022a) and hinders scalability. We extend the backbone of (Gao et al., 2022a) from 2D to 3D medical images by adding an extra dimension channel *i.e.*, depth. This modification allows us to process visual tokens only on transformer layers, enhancing computational efficiency and scalability. The ablation study confirming the effectiveness of this approach is presented in Section 4.7.1.

**Overall objective function.** Our proposed MiM framework, as illustrated in Algorithm 1, introduces a hierarchically designed approach to 3D medical image representation learning through multi-level reconstruction  $\mathcal{L}_R$  and cross-level alignment  $\mathcal{L}_C$ . We empirically set the level of masked volume to  $L = 3$  in this paper since the three-level masked volume can provide a good balance between the representation learning and computational efficiency. Abalton study of the level of masked volume  $L$  is on the Section 4.7.1. Specifically, the multi-level reconstruction loss in Eq. 2 can be further expanded as follows:

$$\mathcal{L}_R = \mathcal{L}_R^1 + \mathcal{L}_R^2 + \mathcal{L}_R^3. \quad (8)$$

Then, since cross-level alignment loss applied between adjacent level volumes, Eq. 6 can be also further expanded as follows:

$$\mathcal{L}_C = \mathcal{L}_C^{1,2} + \mathcal{L}_C^{2,3}. \quad (9)$$

Thus, the total loss function  $\mathcal{L}$  is the combination of these two losses, as shown in Eq. 10,

$$\mathcal{L} = \mathcal{L}_R + \alpha \mathcal{L}_C, \quad (10)$$

where the hyperparameters  $\alpha$  are used to balance the relative contributions of these two kinds of losses. We empirically set the  $\alpha$  to 0.1 based on our experiment results. The ablation study of hyperparameter  $\alpha$  presents in Section 4.7.2.

---

#### Algorithm 1: MiM: Mask in Mask Self-Supervised Pre-training framework

---

```

input :
1  $\mathcal{D}, \tau$       dataset and the transformations;
2  $\theta, s_\theta$     initial parameters for encoder, encoder;
3  $\xi, d_\xi$     initial parameters for decoder, decoder;
4  $\iota, \mathcal{H}$      initial parameters for aggregation and projector
           heads;
5 optimizer   optimizer, updated parameters via gradient
           backwards;
6  $K, B, \mu$    pre-training steps, batch size and learning rate;
7 for  $k \leftarrow 1$  to  $K$  do
   // sample one batches from dataset
8    $\mathcal{B} \leftarrow \{\{x\} \sim \mathcal{D}\}_{i=1}^B$  for  $i, x \in \mathcal{B}$  do
9     Apply multi-level masked volume generation for  $x$  to
       obtain  $x^1, x^2$  and  $x^3$ ;
10    Apply Eq.(2) for  $x^1$  to obtain  $\mathcal{L}_R^1$  with  $s_\theta$  and  $d_\xi$ ;
11    Apply Eq.(2) for  $x^2$  to obtain  $\mathcal{L}_R^2$  with  $s_\theta$  and  $d_\xi$ ;
12    Apply Eq.(2) for  $x^3$  to obtain  $\mathcal{L}_R^3$  with  $s_\theta$  and  $d_\xi$ ;
13    Apply Eq.(3) to obtain  $\mathcal{L}^R$  with  $s_\theta$  and  $d_\xi$ ;
14    Apply Eq.(6) for  $x^2$  and  $x^1$  to obtain  $\mathcal{L}_C^{1,2}$  with  $s_\theta$  and
        $\mathcal{H}_i$ ;
15    Apply Eq.(6) for  $x^3$  and  $x^2$  to obtain  $\mathcal{L}_C^{2,3}$  with  $s_\theta$  and
        $\mathcal{H}_i$ ;
16    Apply Eq.(7) to obtain  $\mathcal{L}^C$  with  $s_\theta$  and  $\mathcal{H}_i$ ;
17    Apply Eq.(10) to obtain the final loss  $\mathcal{L}$ 
18     $\delta\theta \leftarrow \frac{1}{B} \sum_{i=1}^B (\partial_\theta \mathcal{L})$ ;  $\delta\xi \leftarrow \frac{1}{B} \sum_{i=1}^B (\partial_\xi \mathcal{L})$ ;
19     $\delta\iota \leftarrow \frac{1}{B} \sum_{i=1}^B (\partial_\iota \mathcal{L})$ ;
20     $\theta \leftarrow \text{optimizer}(\theta, \delta\theta, \mu)$ ;  $\xi \leftarrow \text{optimizer}(\xi, \delta\xi, \mu)$ ;
21     $\iota \leftarrow \text{optimizer}(\iota, \delta\iota, \mu)$ ;
output :  $s_\theta$  // the pre-trained backbone encoder

```

---

## 4. Experiments

This section will commence by introducing the pre-training datasets, downstream datasets, and evaluation metrics. Subsequently, we will elaborate on the implementation details of our MiM. Lastly, we will present the experimental results of MiM in comparison to other SOTA methods on various tasks and datasets, along with an analysis of our proposed approach.

### 4.1. Datasets and Evaluation

**Pre-training datasets.** To conduct a fair comparison with previous works (Chen et al., 2023b; Tang et al., 2022; He et al., 2023; Wang et al., 2023d; Xie et al., 2022a; Zhou et al., 2021c,b, 2023; Zhuang et al., 2023b), we also carried out pre-training experiments on two public datasets, *i.e.*, BTCV (Landman et al.,

**Table 1. The details of each clinical dataset in our pre-training datasets.**

Datasets	Region of Interest	Pre-training		#Samples	Pre-processing
		1k	10k		
BTCV (Landman et al., 2015)	Abdomen	✓	✓	24	1. Change the volumetric orientation based on the given settings, <i>e.g.</i> , RAS 2. Clip intensity value to [-1000, 1000] and normalize to the range of [0, 1]. 3. Pad each dimension with 0 to meet the minimum shape of input. 4. Randomly crop the sub-volume with the specific shape $H_1 \times W_1 \times D_1$
TCIA Covid19 (An et al., 2020)	Chest	✓	✓	722	
LUNA16 (Harmon et al., 2020)	Chest		✓	843	
STOIC 2021 (Revel et al., 2021)	Chest		✓	2,000	
FLARE23	Abdomen		✓	4,000	
LiDC (Armato III et al., 2011)	Chest		✓	589	
HNSCC (Grossberg et al., 2018)	Head/Neck		✓	1,071	
TotalSegmentator (Wasserthal et al., 2022)	Head/Neck/Chest/leg		✓	1,203	
	Abdomen/pelvis/feet		✓		
<b>Total</b>				10,502	

2015) and TCIA Covid19 (Clark et al., 2013), and combined them to form a new dataset named **1k**. Additionally, to explore the scaling ability of our proposed method compared to previous state-of-the-art methods (Chen et al., 2023b; Tang et al., 2022), we collected eight publicly accessible 3D medical image datasets consisting of 10,502 CT scans to establish our pre-training datasets, which we named **10k**. It is important to note that **10k** is only used for exploring the scaling ability of our proposed method, while we mainly focus on the **1k** dataset for fair comparison and analysis of our proposed method. Table 1 provides a summary of the sources of each collected dataset. Our pre-training process solely utilizes volumetric images without involving any annotations from any of these datasets.

**Downstream datasets.** To evaluate the effectiveness of our MiM, we conduct experiments on thirteen public datasets, *i.e.*, BTCV (Landman et al., 2015), MM-WHS (Ji et al., 2022), Spleen (Simpson et al., 2019), Flare22 (Ma et al., 2023), Amos22 (Ji et al., 2022), MSD Task03 (Simpson et al., 2019), MSD Task06 (Simpson et al., 2019), MSD Task07 (Simpson et al., 2019), MSD Task08 (Simpson et al., 2019), MSD Task10 (Simpson et al., 2019), Covid-19-20 (Roth et al., 2022), BrasTS 21 (Simpson et al., 2019), and CC-CCII (Zhang et al., 2020). These datasets include segmentation and classification tasks, with the first ten datasets used for organ segmentation, the eleventh dataset used for lesion segmentation, the twelfth dataset used for tumor segmentation, and the last dataset used for disease classification. Table 2 provides a summary of the details of each clinical dataset used in our downstream tasks. It’s noted that BTCV (Landman et al., 2015) is used in pre-training, the other datasets are unseen in pre-training. Furthermore, to evaluate the cross-modality generalization ability, we transferred the model pre-trained on CT scans to the MRI dataset BrasTS 21 (Simpson et al., 2019). We adopted consistent settings as previous work (Chen et al., 2023b; He et al., 2023; Tang et al., 2022; Zhuang et al., 2023b).

**Evaluation metrics.** Following (Chen et al., 2023b; Tang et al., 2022; Zhuang et al., 2023b), we utilized the Dice Similarity Coefficient (DSC)<sup>1</sup>, and Normalized Surface Distance (NSD)<sup>2</sup> to assess the performance on segmentation tasks. We then utilized

<sup>1</sup><https://docs.monai.io/en/latest/metrics.html#mean-dice>

<sup>2</sup><https://docs.monai.io/en/latest/metrics.html#monai.metrics.SurfaceDiceMetric>

Accuracy (ACC) and the Area Under the Curve (AUC)<sup>3</sup> for accessing performance on disease classification.

#### 4.2. Implementation Details and Evaluation metrics

**Implementation details.** In the pre-training process, we followed the settings of previous works (Chen et al., 2023b; Tang et al., 2022; Wang et al., 2023d) and provided the details of our MiM pre-training settings in Table 3. We used the backbone of (Gao et al., 2022a) as the encoder for efficient token processing. As previous SSL (Caron et al., 2021; Zhuang et al., 2023b), the prediction head and projection head are implemented with MLP layers for aligning the dimension. In the downstream process, we used Swin-UNETR (Hatamizadeh et al., 2021) for fine-tuning on segmentation tasks and Swin-ViT for fine-tuning on classification tasks, as per the settings of previous works (Tang et al., 2022; He et al., 2023; Wang et al., 2023d). We initialized the encoder of the network with learned parameters in the pre-training process and fine-tuned the overall network. We used the AdamW (Kingma and Ba, 2014) optimizer with a cosine learning rate scheduler for all experiments. For inference on these datasets, we applied a slicing window inference with overlapping to enable a fair comparison with previous works (Tang et al., 2022; Wang et al., 2023d). All methods were pre-trained on four NVIDIA 3090Ti and then fine-tuned on a single NVIDIA 3090Ti. It is important to note that for evaluating the pure effectiveness of our proposed method, we did not use any foundation model or post-processing techniques (Jiang et al., 2023; Liu et al., 2023b).

**Comparison methods.** In our experiments, we compared our proposed MiM method with both General SSL and Medical SSL methods. First, we compare the typical SSL methods MoCov3 (Chen et al., 2021c) and MAE (Chen et al., 2023b; He et al., 2022), since they represent the two mainstream SSL paradigms, *i.e.*, Contrastive learning and Pretext task. We also report the results of SimCLR (Chen et al., 2020a) and PL (Zhang and Gong, 2023), Jigsaw (Chen et al., 2021a) according to (Chen et al., 2023b; Zhuang et al., 2023b). We further evaluate the performance of SimMIM (Xie et al., 2022b), HPM (Wang et al., 2023d), localMIM (Chen et al., 2023b) and

<sup>3</sup><https://docs.monai.io/en/latest/metrics.html#area-under-the-roc-curve>

**Table 2. The details of each clinical datasets in our downstream datasets.**

Datasets	Regions of Interest	Modality	#Samples	Pre-processing
BTCV (Landman et al., 2015)	Chest	CT	30	1. Resample the resolution to [1.5mm, 1.5mm, 2.0mm] 2. Crop the foregrounds with $96 \times 96 \times 96$ and normalize via HU range [-175, 250] 3. Random flip, rotation and intensities shifting with probabilities of 0.1, 0.1 and 0.5
MM-WHS (Zhuang, 2018)	Heart	CT	20	1. Resample the resolution to [1.5mm, 1.5mm, 1.5mm] 2. Crop the foregrounds with $96 \times 96 \times 96$ and normalize via HU range [0, 1700]
Spleen (Simpson et al., 2019)	Spleen	CT	41	1. Resample the resolution to [1.0mm, 1.0mm, 1.0mm] 2. Crop the foregrounds with $96 \times 96 \times 96$ and normalize via [-57, 175] 3. Random flip, rotation and intensities shifting with probabilities of 0.5, 0.25 and 0.5
Amos22 (Zhuang, 2018)	Chest	CT	301	1. Resample the resolution to [1.5mm, 1.5mm, 2.0mm] 2. Crop the foregrounds with $96 \times 96 \times 96$ and normalize via [-175, 250] 3. Random flip, rotation and intensities shifting with probabilities of 0.5, 0.5 and 0.5
Flare22 (Zhuang, 2018)	Chest	CT	50	1. Resample the resolution to [1.5mm, 1.5mm, 2.0mm] 2. Crop the foregrounds with $96 \times 96 \times 96$ and normalize via [-175, 250] 3. Random flip, rotation and intensities shifting with probabilities of 0.2, 0.2 and 0.1
MSD Task03 (Simpson et al., 2019)	Liver	CT	125	1. Resample the resolution to [1.0mm, 1.0mm, 1.0mm] 2. Crop the foregrounds with $96 \times 96 \times 96$ and normalize via HU range [-21, 189] 3. Random flip, rotation and intensities shifting with probabilities of 0.2, 0.2 and 0.1
MSD Task06 (Simpson et al., 2019)	Lung	CT	63	1. Resample the resolution to [1.0mm, 1.0mm, 1.0mm] 2. Crop the foregrounds with $96 \times 96 \times 96$ and normalize via [-1000, 1000] 3. Random flip, rotation and intensities shifting with probabilities of 0.5, 0.3 and 0.1
MSD Task07 (Simpson et al., 2019)	Pancreas	CT	281	1. Resample the resolution to [1.5mm, 1.5mm, 1.5mm] 2. Crop the foregrounds with $96 \times 96 \times 96$ and normalize via HU range [-87, 199] 3. Random flip, rotation and intensities shifting with probabilities of 0.5, 0.25 and 0.5
MSD Task08 (Simpson et al., 2019)	Hepatic Vessel	CT	303	1. Resample the resolution to [1.5mm, 1.5mm, 1.5mm] 2. Crop the foregrounds with $96 \times 96 \times 96$ and normalize via HU range [0, 230] 3. Random flip, rotation and intensities shifting with probabilities of 0.5, 0.25 and 0.5
MSD Task10 (Simpson et al., 2019)	Colon	CT	126	1. Resample the resolution to [1.5mm, 1.5mm, 1.5mm] 2. Crop the foregrounds with $96 \times 96 \times 96$ and normalize via HU range [-57, 175] 3. Random flip, rotation and intensities shifting with probabilities of 0.5, 0.25 and 0.5
Covid-19-20 (Roth et al., 2022)	Covid-19 lesion	CT	189	1. Resample the resolution to [1.25mm, 1.25mm, 5.0mm] 2. Crop the foregrounds with $192 \times 192 \times 32$ and normalize via HU range [-1000, 500]
BraTS 21 (Simpson et al., 2019)	Brain tumor	MRI	484	1. Resample the resolution to [1.0mm, 1.0mm, 1.0mm] 2. Crop the foregrounds with $224 \times 224 \times 120$ and normalize via z-score across channels
CC-CCII (Zhang et al., 2020)	Covid-19 diseases	CT	4178	Crop the foregrounds with $384 \times 384 \times 32$ and normalize via min-max normalization

**Table 3. Pre-training settings.**

Pre-training settings	
Steps	45K
Optimizer	AdamW
Learning rate (LR)	1e-4
LR scheduler	cosine annealing schedule
Warmup step	100
Momentum	0.9
Regularization weight	1e-2
Batch size	256
MiM Level-1 $H^1 \times W^1 \times D^1$	$384 \times 384 \times 192$
MiM Level-2 $H^2 \times W^2 \times D^2$	$96 \times 96 \times 96$
MiM Level-3 $H^3 \times W^3 \times D^3$	$16 \times 16 \times 16$
MiM Resize after crop $h \times w \times d$	$96 \times 96 \times 96$
MiM $\beta_1, \beta_2, \beta_3, \beta_4, \beta_5$	1.0, 1.0, 1.0, 0.1, 0.1
MiM mask ratio $\tau$	0.6
MiM sampling times on next level $\gamma$	4

MCMAE (Gao et al., 2022a), since they are related to our advanced hybrid MAE. We also compare with Adam (Hossein-zadeh Taher et al., 2023) due to related to our hierarchical design of multi-granularity. In addition, we compared with most existing state-of-the-art medical SSL methods in our experiments.

### 4.3. Experiments on downstream tasks

#### 4.3.1. Comparison on the BTCV dataset

**Outperform existing methods.** We first conducted experiments on the BTCV (Landman et al., 2015), and the results are presented in Table 4. Among the comparison methods, SimCLR (Chen and He, 2020), MoCov3 (Chen et al., 2021c), DINO (Caron et al., 2021), localMIM (Wang et al., 2023b), HPM (Wang et al., 2023b), MAE3D (Chen et al., 2023b), GL-MAE (Zhuang et al., 2023b) adopted UNETR (Hatamizadeh et al., 2022) as networks architecture. Most other methods, including our MiM, used Swin-UNETR (Hatamizadeh et al., 2021) as per the settings of previous works (Tang et al., 2022).

**Remark.** As shown in Table 4, we observed that General SSL methods performed worse than Medical SSL methods. Specifically, SimCLR (Chen and He, 2020) and MoCov3 (Chen et al., 2021c) achieved only 73.85% and 79.54%, respectively. This is because these methods rely on a large batch size and negative samples to avoid trivial constants, which is impractical for 3D medical images. Additionally, the negative relationship between different images used in SimCLR (Chen and He, 2020; Chen et al., 2020b) and MoCo (He et al., 2020; Chen et al., 2020c, 2021c) is not suitable for 3D medical images. Jigsaw (Chen et al., 2021a) and DINO (Caron et al., 2021) also achieved limited improvements. Our proposed method, MiM, outperformed MAE-based methods such



**Table 4. Experiment results on BTCV dataset (Landman et al., 2015) across thirteen organs. The best results are highlighted in red. The term ‘From Scratch’ signifies the supervised baseline without self-supervised pre-training. Gray rows represent supervised baselines employing the identical backbone as the proposed MiM. † denotes that we re-implement the approach. Most results are drawn from (Chen et al., 2023b; Zhang et al., 2023; Zhuang et al., 2023b) or their papers.**

Method	Pre-training dataset	Dice Score (%)													Avg
		Spl	RKid	LKid	Gall	Eso	Liv	Sto	Aor	IVC	Veins	Pan	RAG	LAG	
<b>From Scratch</b>															
UNETR (Hatamizadeh et al., 2022)	-	93.02	94.13	94.12	66.99	70.87	96.11	77.27	89.22	82.10	70.16	76.65	65.32	59.21	79.82
Swin-UNETR (Hatamizadeh et al., 2021)	-	94.06	93.54	93.80	65.51	74.60	97.09	75.94	91.80	82.36	73.63	75.19	68.00	61.11	80.53
<b>with General SSL</b>															
SimCLR (Chen et al., 2020a)	1k	92.79	93.04	91.41	49.65	50.99	98.49	77.92	85.56	80.58	64.37	67.16	59.04	48.99	73.85
MoCov3 (Chen et al., 2021c)	1k	91.96	92.85	92.42	68.25	72.77	94.91	78.82	88.21	81.59	71.15	75.76	66.48	58.81	79.54
Jigsaw (Chen et al., 2021a)	1k	94.62	93.41	93.55	75.63	73.21	95.71	80.80	89.41	84.78	71.02	79.57	65.68	60.22	81.35
DINO† (Caron et al., 2021)	1k	93.64	92.95	92.77	74.70	71.87	96.47	77.85	89.49	83.30	72.12	78.41	67.26	63.88	81.22
SimMIM (Xie et al., 2022b)	1k	95.51	93.61	93.49	67.91	73.50	96.46	81.15	89.78	84.86	72.45	75.70	66.89	64.46	81.41
localMIM† (Wang et al., 2023b)	1k	95.31	94.16	94.17	74.52	73.69	96.57	82.21	89.92	84.67	72.12	76.89	67.68	62.29	81.96
HPM† (Wang et al., 2023a)	1k	94.47	93.46	93.86	75.62	74.07	96.11	80.92	90.01	84.42	71.25	79.29	67.34	64.40	82.03
MCMAE† (Gao et al., 2022a)	1k	94.60	94.08	93.87	62.66	75.13	96.26	82.08	90.27	85.68	75.99	81.18	68.78	64.68	82.20
<b>with 3D Medical SSL</b>															
ROT (Taleb et al., 2020)	1k	91.75	93.13	91.62	65.09	76.55	94.21	86.16	89.74	83.08	71.13	81.55	67.90	63.72	81.20
Rubik++ (Zhu et al., 2020)	1k	96.21	90.41	89.33	75.22	72.64	97.44	79.25	89.65	83.76	74.74	78.35	67.14	61.97	81.38
ModelGen (Zhou et al., 2021c)	1k	91.99	93.52	91.81	65.11	76.14	95.98	86.88	89.29	83.59	71.79	81.62	67.97	63.18	81.45
PCRLv1† (Zhou et al., 2021b)	1k	94.44	92.50	92.75	56.46	74.95	96.62	81.64	89.86	87.12	72.78	75.24	69.73	68.18	81.30
PCRLv2† (Zhou et al., 2023)	1k	95.50	91.43	89.52	76.15	73.54	97.28	79.64	90.16	84.17	75.20	78.71	68.74	62.93	81.74
SwinMM (Wang et al., 2023d)	1k	94.33	94.18	94.16	72.97	74.75	96.37	83.23	89.56	82.91	70.65	75.52	69.17	62.90	81.81
Adam† (Hosseinzadeh Taher et al., 2023)	1k	94.16	93.65	93.43	66.14	71.28	96.18	76.93	89.83	85.35	71.16	80.37	63.97	60.83	80.45
GVSL† (He et al., 2023)	1k	95.27	91.22	92.25	72.69	73.56	96.44	82.40	88.90	84.22	70.84	76.42	67.48	63.25	81.87
UniMiss† (Xie et al., 2022a)	1k	95.24	93.74	93.78	72.69	73.61	96.23	83.08	88.50	83.31	71.89	78.60	66.22	68.03	82.05
GL-MAE (Zhuang et al., 2023b)	1k	94.54	94.39	94.37	73.19	74.93	96.51	83.49	89.74	83.11	70.80	75.71	69.39	63.12	82.33
Swin-UNETR† (Tang et al., 2022)	1k	95.91	94.48	94.42	69.57	76.47	96.94	78.50	90.31	85.77	75.12	81.33	67.37	64.92	82.58
MAE3D (Chen et al., 2023b)	1k	95.81	94.38	94.48	69.96	76.85	96.69	80.44	90.33	84.33	73.65	80.11	68.65	64.44	82.40
<b>MiM</b>	1k	96.05	94.58	94.53	75.73	77.36	97.03	83.23	90.37	87.64	74.97	82.62	71.02	68.80	84.46
Swin-UNETR† (Tang et al., 2022)	10k	95.20	94.30	94.15	76.53	74.02	96.61	82.25	89.84	84.20	74.23	82.53	70.74	67.49	83.20
MAE3D† (Chen et al., 2023b)	10k	95.91	94.28	94.26	73.82	75.35	97.07	83.53	91.12	86.74	75.13	83.33	68.43	66.40	83.52
<b>MiM</b>	10k	96.37	94.83	94.75	81.02	80.08	97.12	85.30	90.36	87.66	75.99	84.41	71.94	69.64	85.41

Note: Spl: spleen, RKid: right kidney, LKid: left kidney, Gall: gallbladder, Eso: esophagus, Liv: liver, Sto: stomach, Aor: aorta, IVC: inferior vena cava, Veins: portal and splenic veins, Pan: pancreas, AG: left and right adrenal glands.

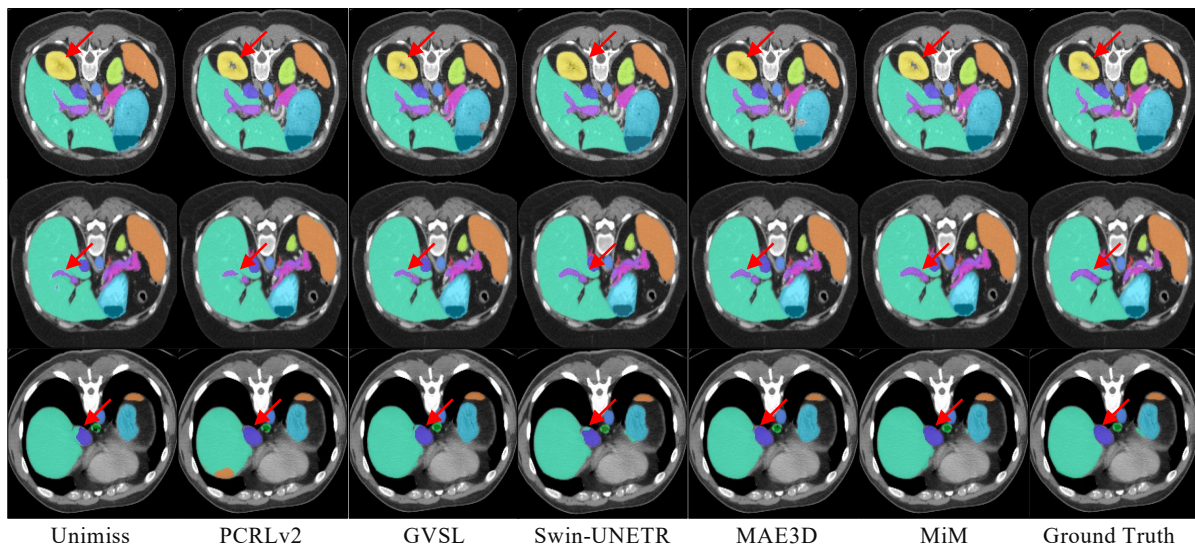


**Fig. 5. Visualization of segmentation results on BTCV validation dataset (Landman et al., 2015). We compared MiM with Unimiss (Xie et al., 2022a), PCRLv2 (Zhou et al., 2023), GVSL (He et al., 2023), Swin-UNETR (Tang et al., 2022) and MAE3D (Chen et al., 2023b).**

as MAE3D (Chen et al., 2023b), GL-MAE (Zhuang et al., 2023b), localMIM (Wang et al., 2023b), HPM (Wang et al., 2023b), and MCMAE (Gao et al., 2022a) by a significant margin. We concluded that General SSL methods are not very suitable for 3D medical images, and it is crucial to consider the characteristics of 3D medical images when designing SSL methods.

The scratch Swin-UNETR (Hatamizadeh et al., 2021) only achieves 80.53% DSC. By pre-training with MiM on a 1k unlabeled dataset, we gained a 3.93% improvement with 84.46% DSC, which outperforms existing methods by a clear margin. Among the compared methods, Swin-UNETR (Tang et al., 2022) and MAE3D (Chen et al., 2023b) achieved the best 82.58% and second-best 82.40% DSC, respectively. Our pro-

**Table 5. Experiment results on BTCV (Landman et al., 2015), MM-WHS (Zhuang, 2018), MSD Spleen (An et al., 2020), Amos22 (Ji et al., 2022) and Flare22 (Ma et al., 2023) with varying ratios of training datasets. The evaluation was conducted using the DSC(%) metric, with Avg representing the mean performance across all datasets under varied conditions. † denotes we re-implement the approach and report the results. Most results are drawn from (Chen et al., 2023b; Zhuang et al., 2023b).**

Method	Pre-training dataset	BTCV			MM-WHS			MSD Spleen			Amos22			Flare22			Avg
		25%	50%	100%	25%	50%	100%	25%	50%	100%	25%	50%	100%	25%	50%	100%	
<i>From scratch</i>																	
UNETR (Hatamizadeh et al., 2022)	-	58.99	75.20	79.82	78.77	85.31	85.85	89.67	92.23	94.20	73.53	81.46	84.34	75.32	76.29	76.94	80.53
Swin-UNETR (Hatamizadeh et al., 2021)	-	63.08	75.38	80.53	79.59	85.65	86.11	90.08	93.29	94.90	76.03	82.60	84.85	77.43	80.50	83.08	82.21
<i>with General SSL</i>																	
SimCLR (Chen et al., 2020a)	1k	59.03	75.31	79.85	78.88	85.52	86.00	89.88	92.52	94.11	73.62	81.65	84.66	75.34	76.33	77.03	80.65
MoCov3† (Chen et al., 2021c)	1k	49.55	75.65	79.54	79.50	86.13	84.16	92.12	93.56	94.23	76.11	82.70	84.95	77.62	80.91	83.22	81.33
Jigsaw (Chen et al., 2021a)	1k	59.83	75.89	81.35	80.51	86.50	89.75	93.23	93.61	94.29	77.43	86.09	87.49	78.01	82.85	86.40	83.55
DINO† (Caron et al., 2021)	1k	59.68	75.53	81.22	78.80	86.31	89.80	93.58	93.84	95.79	74.40	84.43	87.24	78.42	82.01	85.99	83.14
SimMIM† (Xie et al., 2022b)	1k	62.01	75.98	81.41	79.71	86.38	90.22	93.87	93.48	94.94	79.57	86.97	89.74	78.01	82.49	86.05	84.01
localMIM† (Wang et al., 2023b)	1k	62.26	77.43	81.96	82.21	87.15	89.99	91.80	92.48	93.37	79.84	85.72	88.09	78.43	82.42	86.48	83.98
HPM† (Wang et al., 2023a)	1k	62.95	76.32	82.03	82.34	87.64	89.86	93.78	93.11	93.86	79.89	85.70	88.07	78.20	82.42	86.15	84.16
MCMAE† (Gao et al., 2022a)	1k	64.70	78.01	82.20	85.24	88.74	90.29	94.92	95.88	96.04	75.82	84.76	86.63	78.97	80.79	84.31	84.49
<i>with 3D Medical SSL</i>																	
ROT (Taleb et al., 2020)	1k	53.43	74.44	81.20	80.12	86.98	87.12	90.99	95.01	95.45	76.88	86.01	87.12	77.11	81.16	84.51	82.50
Rubik++ (Zhu et al., 2020)	1k	53.00	74.74	81.38	80.88	87.18	88.02	91.91	95.22	95.73	77.43	86.91	88.20	78.43	82.85	86.49	83.22
ModelGen (Zhou et al., 2021c)	1k	54.18	61.26	81.45	80.33	86.26	89.69	92.01	95.22	95.73	77.49	86.20	88.29	78.17	82.37	84.02	82.18
PCRLv1† (Zhou et al., 2021b)	1k	55.08	70.92	81.30	83.34	87.59	90.32	89.69	92.01	95.10	79.46	86.24	86.02	78.44	84.14	87.34	83.13
PCRLv2† (Zhou et al., 2023)	1k	58.67	71.40	81.32	84.51	88.13	90.36	90.32	95.16	95.46	77.32	84.92	88.79	79.10	85.37	87.45	83.89
SwinMIM† (Wang et al., 2023d)	1k	59.40	73.66	81.81	84.61	88.32	90.40	90.36	95.23	95.55	77.33	84.95	88.88	79.26	85.62	87.56	84.20
Adam† (Hosseinzadeh Taher et al., 2023)	1k	64.12	73.66	80.45	83.12	87.26	88.82	88.73	92.09	86.90	59.89	73.89	88.87	79.54	84.43	87.24	81.27
GVSL† (He et al., 2023)	1k	52.03	74.23	81.87	85.24	88.00	90.22	95.36	96.20	96.57	78.72	87.41	89.92	81.89	85.38	87.42	84.70
Unimiss† (Xie et al., 2022a)	1k	65.96	77.15	82.05	83.64	88.49	90.37	93.30	94.74	95.10	77.03	85.08	88.23	80.37	85.21	87.66	84.96
GL-MAE (Zhuang et al., 2023b)	1k	66.44	76.37	82.33	76.16	87.72	88.88	93.65	94.36	95.72	74.65	84.65	87.40	80.20	85.03	87.26	84.05
Swin-UNETR† (Tang et al., 2022)	1k	62.12	76.13	82.58	85.33	87.50	90.32	95.13	95.00	95.02	78.41	87.49	89.83	83.21	85.72	87.17	85.40
MAE3D† (Chen et al., 2023b)	1k	63.66	78.57	82.48	85.57	88.62	90.03	95.12	95.11	95.50	77.63	87.08	89.71	83.31	85.85	87.31	85.70
MiM	1k	70.71	81.22	84.66	86.52	88.99	91.04	95.99	96.42	96.98	80.55	88.94	90.96	85.55	86.29	88.96	87.59
Swin-UNETR† (Tang et al., 2022)	10k	69.96	78.32	83.20	85.88	88.83	90.47	92.30	95.97	96.26	78.15	86.61	89.96	84.54	86.27	88.04	86.32
MAE3D† (Chen et al., 2023b)	10k	70.59	79.44	83.52	85.78	89.13	90.75	95.57	96.19	96.92	77.01	86.94	88.55	84.44	86.27	88.50	86.64
MiM	10k	75.34	81.80	85.61	86.41	89.77	91.12	96.36	96.68	96.99	81.29	89.06	91.60	86.29	87.79	89.67	88.34

posed MiM surpasses these two methods by 1.88% and 2.06% DSC, respectively, which is a clear improvement on this dataset.

It's worth noting that scaling laws (Kaplan et al., 2020; Singh et al., 2023; El-Nouby et al., 2024) also apply to 3D medical image pre-training. By pre-training with our larger scale unlabeled **10k** dataset, we observed that Swin-UNETR and MAE3D achieved DSC scores of 83.20% and 83.52%, respectively. Our proposed MiM with **10k** achieved a DSC score of 85.41%, which consistently outperformed these two methods by a large margin. These results suggest that scaling plays an important role in pre-training for 3D medical images and that our proposed MiM method is effective for pre-training on larger datasets.

**Qualitative results.** MiM was found to improve the completeness of segmentation results, as shown in Fig 5. The results of segmentation using MiM were better than those using Swin-UNETR (Tang et al., 2022), MAE3D (Chen et al., 2023b), Unimiss (Xie et al., 2022a), PCRLv2 (Zhou et al., 2023) and GVSL (He et al., 2023).

#### 4.3.2. Comparison on the Unseen datasets

**Promising generalizability.** We further conduct experiments on unseen datasets in pre-training, *i.e.*, M-WHS (Zhuang, 2018), Spleen (Simpson et al., 2019), Amos22 (Ji et al., 2022), and Flare22 (Ma et al., 2023). The results of these four datasets are shown in Table 5. It can be observed that our MiM consistently outperformed all existing methods with a clear margin, which demonstrates promising generalizability to unseen datasets. Specifically, MiM outperformed existing methods by at least 1.89% DSC on average. By pre-training with a larger scale of unlabeled dataset **10k**, Swin-UNETR (Tang et al.,

2022) and MAE3D (Chen et al., 2023b) improved by 0.92% and 0.94% DSC with 86.32% and 86.64%, respectively. Our MiM also gained improvement to 88.34% DSC and outperformed these two methods consistently.

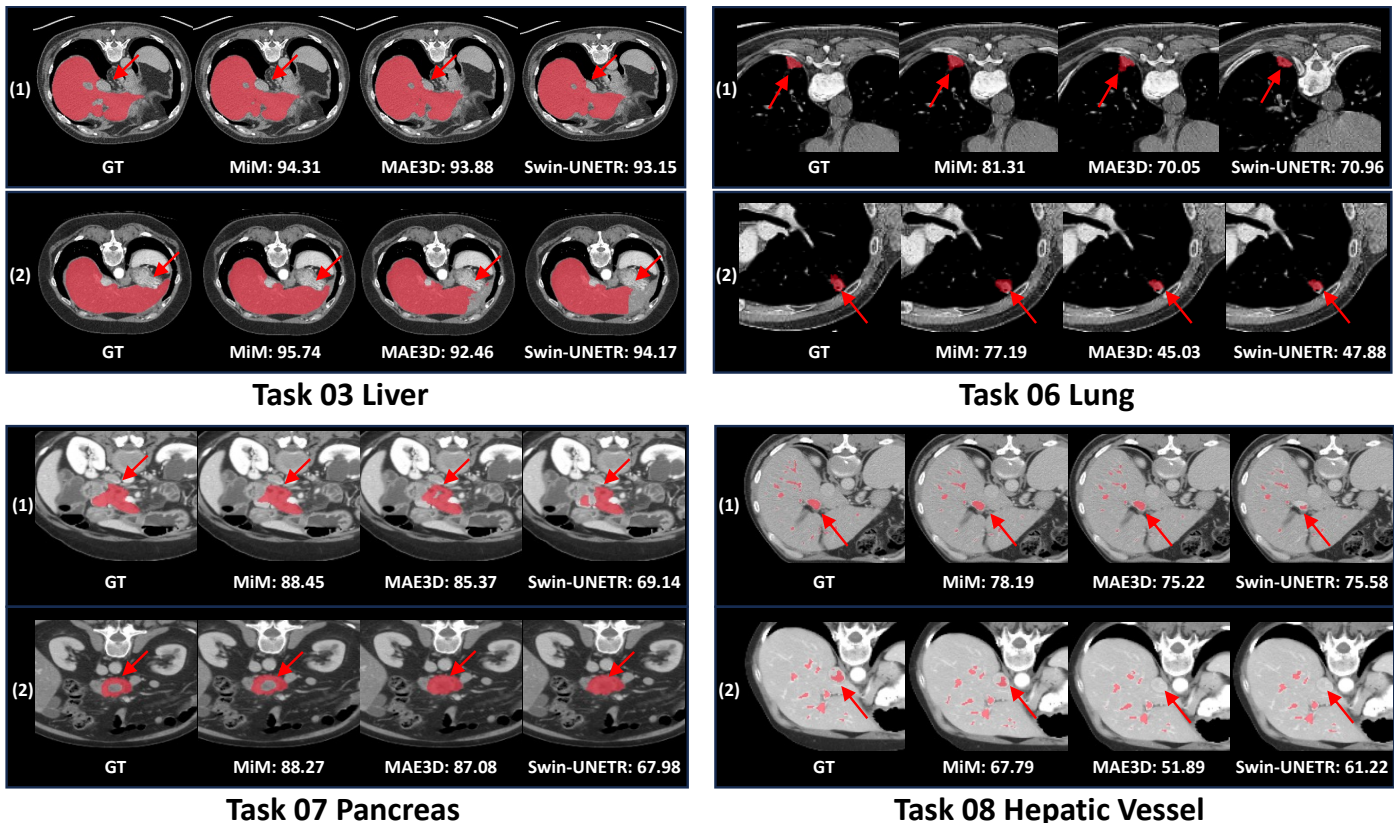
**Qualitative results.** To gain a better understanding of the improvements achieved by MiM, we present the visualization of segmentation results for four tasks on the MSD dataset (Simpson et al., 2019). We compared our MiM method with MAE3D (Chen et al., 2023b) and Swin-UNETR (Tang et al., 2022). It can be observed in Fig. 6 that MiM outperforms MAE3D (Chen et al., 2023b) and Swin-UNETR (Tang et al., 2022), by effectively addressing the issues of under and over-segmentation outliers observed in the segmentation results obtained by these methods. Specifically, Swin-UNETR (Tang et al., 2022) exhibits under-segmentation due to the absence of certain parts of the labels such as the liver and hepatic vessel, leading to a lower DSC. On the other hand, in the case of the pancreas, over-segmentation is observed with MAE3D (Chen et al., 2023b) and Swin-UNETR (Tang et al., 2022), where surrounding tissues are included with the label. In contrast, our proposed MiM method effectively delineates the boundary of the pancreas.

#### 4.4. Comparison on the Covid-19-20 dataset

**Generalization capacity on Lesion Segmentation task.** To evaluate the generalizability of our MiM on the lesion segmentation task, we conducted experiments on the Covid-19-20 (Zhang et al., 2020) dataset. Lesion segmentation involves identifying specific abnormalities, unlike organ segmentation that focuses on delineating anatomical structures (Simpson et al., 2019; Zhang et al., 2020). showed that our pro-

**Table 6. Experiment results on Task03 Liver, Task06 Lung, Task07 Pancreas, Task08 Hepatic Vessel and Task10 Colon on MSD dataset (Simpson et al., 2019).**

Method	Pre-training dataset	Network	Task03 Liver		Task06 Lung		Task07 Pancreas		Task08 Hepatic Vessel		Task10 Colon		Avg	
			DSC(%)	NSD(%)	DSC(%)	NSD(%)	DSC(%)	NSD(%)	DSC(%)	NSD(%)	DSC(%)	NSD(%)	DSC(%)	NSD(%)
<i>From scratch</i>														
3D UNet (Ronneberger et al., 2015)	-	-	94.41	93.94	48.09	42.65	75.33	90.98	56.11	77.58	40.97	54.63	62.98	71.95
UNETR (Hatamizadeh et al., 2022)	-	-	94.27	94.00	44.26	40.74	74.12	88.79	58.45	79.34	27.39	42.55	59.70	69.08
Swin-UNETR (Hatamizadeh et al., 2021)	-	-	94.52	94.08	51.97	48.68	75.75	88.87	57.24	77.84	44.57	56.15	64.84	73.12
<i>with General SSL</i>														
MoCov3 (Chen et al., 2021c)	1k	UNETR	94.15	93.22	52.11	48.16	74.16	78.13	58.11	78.13	43.99	55.13	64.90	72.55
localMIM (Wang et al., 2023b)	1k	UNETR	94.72	93.69	52.93	48.75	74.74	79.77	58.86	78.77	44.52	54.35	65.55	73.10
HPM (Wang et al., 2023b)	1k	UNETR	94.63	93.25	53.63	48.34	74.74	78.13	59.89	78.93	42.67	55.13	65.51	72.81
SimMIM (Xie et al., 2022b)	1k	Swin-UNETR	94.50	92.45	56.93	52.41	74.99	79.77	60.44	78.99	42.42	54.35	66.26	73.65
MCMMAE (Gao et al., 2022a)	1k	Swin-UNETR	95.49	94.33	57.08	57.18	75.78	78.13	60.44	78.93	45.63	55.13	67.28	74.96
<i>with 3D Medical SSL</i>														
ModelGen (Zhou et al., 2021c)	1k	3D UNet	94.49	94.22	56.26	51.80	76.92	91.70	58.28	78.34	47.15	58.08	66.68	74.83
PCRLv2 (Zhou et al., 2023)	1k	3D UNet	94.61	95.78	62.57	59.67	77.02	92.67	53.63	76.25	39.78	53.50	65.52	75.57
GL-MAE (Zhuang et al., 2023b)	1k	UNETR	94.65	93.48	53.28	49.51	72.96	87.90	60.26	78.65	45.52	59.45	65.53	74.20
MAE3D (Chen et al., 2023b)	1k	UNETR	95.53	96.62	58.30	52.32	77.31	91.92	60.44	78.80	45.40	56.00	66.76	75.33
Rubik++ (Zhu et al., 2020)	1k	Swin-UNETR	94.49	94.22	56.43	52.84	76.14	90.88	60.42	78.71	40.49	50.78	65.63	73.69
GVSL (He et al., 2023)	1k	Swin-UNETR	95.62	95.78	59.44	54.59	77.82	92.61	57.74	77.93	50.55	61.42	68.23	76.76
Swin-UNETR (Tang et al., 2022)	1k	Swin-UNETR	95.55	96.61	60.23	57.22	76.93	90.88	60.44	79.08	43.21	55.43	68.98	75.16
MiM	1k	UNETR	96.01	97.03	63.06	60.11	78.39	92.71	60.71	79.44	51.02	62.57	69.79	78.37
MiM	1k	Swin-UNETR	96.14	97.43	63.52	60.92	78.86	92.80	60.85	79.55	51.02	63.03	70.07	78.75
MiM	10k	Swin-UNETR	96.41	97.63	64.46	62.59	79.19	93.14	61.72	80.06	52.73	64.85	70.76	79.67

**Fig. 6. Visualization of segmentation results for four tasks on the MSD dataset (Simpson et al., 2019). We compared MiM with MAE3D (Chen et al., 2023b), and Swin-UNETR (Tang et al., 2022). The Dice Score (%) is provided for each segmented volume.**

posed MiM method consistently exhibited performance improvements compared to other SSL methods by at least 1.52% and 1.73% in terms of DSC and NSD, respectively, which is a clear improvement on this dataset. By pre-training with a larger scale of unlabeled dataset **10k**, MiM further improved to 71.11% and 72.42% in DSC and NSD, respectively. These results demonstrate that MiM is effective for lesion segmentation tasks.

#### 4.5. Comparison on CC-CCII dataset

**Generalization capacity on Disease Classification task.** To evaluate the generalizability of our MiM on classification task,

we fine-tuned it on the CC-CCII (Zhang et al., 2020) dataset and compared its performance with state-of-the-art general and medical SSL methods. Since existing SSL methods didn't conduct experiments on this dataset, we reproduced the related methods and reported the results. As shown in Table 8, it can be observed that MiM achieved the best performance in terms of ACC and AUC, surpassing all other methods with 93.63% and 99.39%. These findings demonstrate that the learned representation by MiM can be well transferable to classification problems and can be used effectively for medical image classification tasks. With a larger scale of pre-training dataset **10k**,

**Table 7. Experiment results on Covid-19-20 lesion segmentation dataset (Roth et al., 2022).** † denotes our implementation. Most results are drawn from (Zhuang et al., 2023b) and other own papers.

Method	Pre-training dataset	Network	Lesion segmentation	
			DSC(%)	NSD(%)
<i>From scratch</i>				
SegResNet (Myronenko, 2019)	-	-	61.38	61.73
3D UNet Ronneberger et al. (2015)	-	-	60.35	61.27
UNETR (Hatamizadeh et al., 2022)	-	-	58.80	57.22
Swin-UNETR (Hatamizadeh et al., 2021)	-	-	61.89	61.92
<i>with General SSL</i>				
MoCov3 (Chen et al., 2021c)	1k	UNETR	63.15	64.32
localMIM (Wang et al., 2023b)	1k	UNETR	66.62	67.11
simMIM (Xie et al., 2022b)	1k	Swin-UNETR	67.22	68.19
MCMAE† (Gao et al., 2022a)	1k	Swin-UNETR	68.01	68.61
<i>with Medical SSL</i>				
Adam (Hosseinizadeh Taher et al., 2023)	1k	SegResNet	67.31	67.56
ModelGen (Zhou et al., 2021c)	1k	3D UNet	68.25	69.63
PCRLv1 (Zhou et al., 2021b)	1k	3D UNet	67.25	68.14
PCRLv2 (Zhou et al., 2023)	1k	3D UNet	68.18	69.18
GL-MAE (Zhuang et al., 2023b)	1k	UNETR	67.11	68.94
MAE3D† (Chen et al., 2023b)	1k	UNETR	67.86	69.29
Rubik++ (Zhu et al., 2020)	1k	Swin-UNETR	64.60	65.00
Adam† (Hosseinizadeh Taher et al., 2023)	1k	Swin-UNETR	68.01	67.95
SwinMM† (Wang et al., 2023d)	1k	Swin-UNETR	68.11	69.01
GVSL† (He et al., 2023)	1k	Swin-UNETR	68.31	68.28
Swin-UNETR† (Tang et al., 2022)	1k	Swin-UNETR	68.92	69.28
MiM	1k	Swin-UNETR	70.14	71.02
MiM	10k	Swin-UNETR	71.11	72.42

our MiM further improved to 94.12% and 99.52% in ACC and AUC, respectively, which shows the scalability of our proposed method when transferring across tasks.

**Table 8. Experiment results on CC-CCII dataset (Zhang et al., 2020).**

Method	Pre-training dataset	Network	Disease classification	
			ACC(%)	AUC
<i>From Scratch</i>				
ResNet (He et al., 2016)	-	-	85.94	87.61
ViT (Dosovitskiy et al., 2020)	-	-	85.92	96.26
Swin-ViT (Liu et al., 2021)	-	-	87.15	97.32
<i>with General SSL</i>				
SimCLR (Chen et al., 2020a)	1k	ResNet	87.12	96.21
MoCov2 (Chen et al., 2020c)	1k	ResNet	87.01	95.49
localMIM (Wang et al., 2023b)	1k	ViT	88.15	97.58
HPM (Wang et al., 2023a)	1k	ViT	88.26	97.65
Jigsaw (Chen et al., 2021a)	1k	Swin-ViT	87.18	96.89
SimMIM (Xie et al., 2022b)	1k	Swin-ViT	89.62	98.16
MCMAE (Gao et al., 2022a)	1k	Swin-ViT	90.26	97.12
<i>with Medical SSL</i>				
PCRLv1 (Zhou et al., 2021b)	1k	ResNet	88.84	97.69
PCRLv2 (Zhou et al., 2023)	1k	ResNet	89.35	98.05
GL-MAE (Zhuang et al., 2023b)	1k	ViT	88.00	96.97
MAE3D (Chen et al., 2023b)	1k	ViT	91.30	98.13
Rubik++ (Zhu et al., 2020)	1k	Swin-ViT	89.93	98.55
SwinMM (Wang et al., 2023d)	1k	Swin-ViT	89.99	98.77
Swin-UNETR (Tang et al., 2022)	1k	Swin-ViT	91.81	98.97
MiM	1k	Swin-ViT	93.63	99.39
MiM	10k	Swin-ViT	94.26	99.69

#### 4.6. Comparison on the BraTS 21 dataset

**Generalization capacity on MRI modality dataset.** To evaluate the generalizability of our MiM on MRI datasets, we fine-tuned it on the BraST 21 (Simpson et al., 2019) MRI tumor segmentation dataset and compared its performance with state-of-the-art general and medical SSL methods. It can be observed in Table 9 that both SSL methods can improve the performance of the model in segmenting tumors in BrasTS 21 (Simpson et al., 2019) dataset. This is because CT and MRI are often used for the same task but for different purposes, and thus share similar anatomical structures. Therefore, the knowledge learned by SSL methods from unlabeled CT datasets can be transferred to MRI datasets (Lyu and Wang, 2022; Tang et al., 2022). Our MiM outperformed all other methods by at least 1.34% with 79.28% DSC. By pre-training with a larger unlabeled dataset

**10k**, our MiM further improved to 79.92%, which shows the scalability of our proposed method when transferring across modalities.

**Table 9. Experiment results on BraTS-21 (Simpson et al., 2019).** WT, TC, and ET denote the whole tumor, tumor core, and enhancing tumor, respectively. † denotes our implementation.

Method	Pre-training dataset	Network	Dice Score(%)			
			TC	WT	ET	AVG
<i>From Scratch</i>						
UNETR (Hatamizadeh et al., 2022)	-	-	81.62	87.81	57.34	75.58
Swin-UNETR (Hatamizadeh et al., 2021)	-	-	81.28	88.67	57.73	75.89
<i>with General SSL</i>						
SimCLR (Chen et al., 2020a)	1k	UNETR	83.13	89.44	58.42	76.99
MoCov3 (Chen et al., 2021c)	1k	UNETR	82.60	88.89	57.69	76.39
localMIM† (Wang et al., 2023b)	1k	UNETR	82.44	88.78	58.64	76.62
Jigsaw (Chen et al., 2021a)	1k	Swin-UNETR	81.62	89.45	59.10	76.72
SimMIM† (Xie et al., 2022b)	1k	Swin-UNETR	84.06	90.43	59.07	77.85
MCMAE† (Gao et al., 2022a)	1k	Swin-UNETR	84.27	90.52	59.04	77.94
<i>with 3D Medical SSL</i>						
GL-MAE (Zhuang et al., 2023b)	1k	UNETR	82.80	90.65	60.46	77.97
MAE3D† (Chen et al., 2023b)	1k	UNETR	82.34	90.35	59.18	77.29
PCRLv1 (Zhou et al., 2021b)	1k	Swin-UNETR	81.96	88.83	57.58	76.12
PCRLv2 (Zhou et al., 2023)	1k	Swin-UNETR	82.13	90.06	57.70	76.63
Rubik++ (Zhu et al., 2020)	1k	Swin-UNETR	84.32	90.23	58.01	77.51
Swin-UNETR (Tang et al., 2022)	1k	Swin-UNETR	82.51	89.08	58.15	76.58
SwinMM (Wang et al., 2023d)	1k	Swin-UNETR	83.48	90.47	58.72	77.56
MiM	1k	Swin-UNETR	84.99	91.92	60.94	79.28
MiM	10k	Swin-UNETR	85.96	92.34	61.45	79.92

**Label efficiency.** The scarcity of labeled 3D medical images can pose a significant challenge, requiring models to perform well despite this constraint (Tang et al., 2022). To evaluate the effectiveness of MiM under this constraint, we compared it with existing methods by reducing the number of manual labels at label ratios of 25% and 50%. As shown in Table 5. MiM outperformed all other methods by a significant margin when generalized to both BTCV (Landman et al., 2015) and unseen datasets. Specifically, MiM with 50% label achieved comparable performance with the scratch Swin-UNETR with 100% label with a clear margin.

#### 4.6.1. Comparison on the MSD datasets

**Generalizability to Organ Segmentation.** To evaluate the generalizability, we conducted experiments on the five CT-based tasks on the MSD dataset (Simpson et al., 2019), i.e., Task 03 Liver, Task06 Lung, Task07 Pancreas, Task08 Hepatic Vessel and Task10 Colon. Since existing methods didn't conduct experiments with the same pre-training dataset, we reimplemented these methods for fair comparison. It can be observed in Table 6 that MiM achieves the best average DSC (70.07%) and NSD(78.75%) in all tasks. Since the scrtach Swin-UNETR (Hatamizadeh et al., 2021) performs better UNETR (Hatamizadeh et al., 2022) in terms of avg DSC (64.84% vs 62.98%) and NSD (73.12% vs 69.08). We further pre-trained UNETR (Hatamizadeh et al., 2022) based on MiM for a fair comparison. It can be observed that with MiM pre-training, Swin-UNETR (Hatamizadeh et al., 2021) gained an average improvement 5.23% and 5.63% in terms of DSC and NSD, respectively. With UNETR (Hatamizadeh et al., 2022) as the network, we observed an average improvement of 10.09% and 9.29% in terms of DSC and NSD, respectively. Moreover, by pre-training with a larger scale of unlabeled dataset **10k**, MiM further improved to 70.76% and 79.67% in DSC and NSD, respectively. These results demonstrate that MiM is effective for organ segmentation tasks.

#### 4.7. Analysis of our proposed method

We first conducted ablation studies on loss functions and settings of MiM. Then, we conducted a hyper-parameter analysis for the loss terms. Lastly, we provided reconstruction results. All the models were pre-trained on *Ik*, which were then evaluated on BTCV (Landman et al., 2015) and MM-WHS (Zhuang, 2018).

##### 4.7.1. Ablation study

**Loss functions.** To investigate the impact of hierarchical design by applying multi-level reconstruction and cross-level alignment, we conducted a comprehensive ablation study of the loss terms. Table 10 presents the results of the ablation studies on three validation datasets. By utilizing multi-level reconstruction, the model significantly improved upon the previous MiM method, as the model was able to capture multi-granularity visual cues of the 3D medical images and learn representation hierarchically, thereby learning broader information. The cross-level alignment for coarse  $x^1$  and  $x^2$  (4th row) achieved better performance than that of fine-cropped  $x^3$  3D medical images (5th row). Combining all losses could result in best performance improvements.

**Table 10. Evaluation of the loss terms  $\mathcal{L}_R$  and  $\mathcal{L}_C$ . We report the performance on BTCV (Landman et al., 2015), MM-WHS (Zhuang, 2018), and Spleen (Simpson et al., 2019) dataset.**

Loss					BTCV		MM-WHS	
$\mathcal{L}_1^R$	$\mathcal{L}_2^R$	$\mathcal{L}_3^R$	$\mathcal{L}_1^C$	$\mathcal{L}_2^C$	DSC(%)	NSD(%)	DSC	NSD(%)
✗	✗	✗	✗	✗	81.49	75.92	89.42	73.06
✓	✗	✗	✗	✗	83.10	79.51	90.44	74.53
✓	✓	✗	✗	✗	84.25	81.29	90.74	75.50
✓	✓	✓	✗	✗	84.29	81.45	90.89	75.97
✓	✓	✓	✓	✗	84.43	81.56	90.89	76.27
✓	✓	✓	✓	✓	84.66	82.11	91.04	76.65

**Numbers of levels.** We limit the number of levels  $L$  to three. As illustrated in Fig. 7, we varied the number of levels  $L$  and observed that the optimal performance was achieved when  $L = 3$ . This choice stems from the fact that the resolution of the volume at Level-4 is considerably smaller in scale compared to the original volume ( $1 \times 1 \times 1$ ), facilitating easier reconstruction but resulting in suboptimal performance (He et al., 2022; Xie et al., 2022b). Moreover, the proximity of positive patches to negative patches within a confined region may hinder effective discrimination, particularly concerning hard negative patches (Kalandidis et al., 2020). Thus, we set the number of levels  $L = 3$  as the default choice.

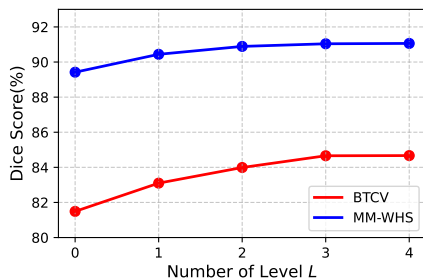


**Fig. 7. Evaluation of the number of level  $L$  for our multi-level volume generation. We report the results on BTCV (Landman et al., 2015) and MM-WHS (Zhuang, 2018).**

**Reconstruction targets for  $\mathcal{L}_R$ .** In Fig. 3, we employ the *mask patches* from the coarser as the finer level volume, which is the

default choice in MiM. In Table 11, we observed that adopting mask patches from the coarser level as the finer level volume results in better performance than the other choices.

**Table 11. Evaluation of the process of finer level volume. We report the DSC on BTCV (Landman et al., 2015) and MM-WHS (Zhuang, 2018).**

Finer level volume	BTCV		MM-WHS	
	DSC(%)	NSD(%)	DSC(%)	NSD(%)
Visible patches	82.18	76.22	89.33	73.65
Maked patches	84.66	82.11	91.04	76.65

**Negative pairs for  $\mathcal{L}_C$ .** In Eq. 6, we employ infoNCE loss (Chen et al., 2020a) as the default choice. This loss maximizes the similarity between the cross-level images and pushes away the negative samples. Another loss function is BYOL cosine loss (Grill et al., 2020). The primary distinction is whether to use negative samples. As demonstrated in Table 12, negative samples aid in learning better representations (Chen et al., 2020c), and thus, we include them in our default choices.

**Table 12. Evaluation of  $\mathcal{L}_C$  whether using negative samples. We report the DSC on BTCV (Landman et al., 2015) and MM-WHS (Zhuang, 2018).**

Loss function $\mathcal{L}_C$	BTCV		MM-WHS	
	DSC(%)	NSD(%)	DSC(%)	NSD(%)
BYOL-style cosine loss (Grill et al., 2020)	83.68	80.12	90.53	74.66
Contrastive loss (Chen et al., 2020a)	84.66	82.11	91.04	76.65

**Efficiency of MiM.** Table 13 presents a comparative analysis of computation costs *i.e.* flops and times during the pre-training period across various methodologies. Our evaluation highlights the computational efficiency of MAE-based approaches when coupled with UNETR, as they leverage only the visible tokens from masked 3D medical images. In contrast, alternative MAE-based methods naively cooperating with hybrid backbones such as Swin-UNETR, necessitate processing all tokens. Our proposed method extends the hybrid backbone architecture (Gao et al., 2022a) to 3D medical images in the pre-training stage, achieving significantly superior performance while maintaining computational efficiency.

**Table 13. Evaluation of model complexity during pre-training and subsequent performance on downstream tasks. We report flops and pre-training duration for pre-training. We report Dice Score(%) on BTCV (Landman et al., 2015) and MM-WHS (Zhuang, 2018) dataset for fine-tuning.**

Method	Networks	Tokens		flops(G)	Pre-training duration	BTCV	MM-WHS
		All	Partial				
MAE3D	UNETR		✓	12.3	9	82.20	90.03
HPM	UNETR		✓	34.1	9.9	82.04	89.86
localMiM	UNETR		✓	26.6	10.3	81.38	89.99
Adam	Swin-UNETR	✓		43.7	27.0	80.45	88.82
SimMiM	Swin-UNETR	✓		70.8	26.6	82.24	90.22
Swin-UNETR	Swin-UNETR	✓		394.84	130.0	82.58	90.32
MiM	Swin-UNETR		✓	45.8	14.6	84.66	91.04

##### 4.7.2. Hyper-parameter analysis

**Weights of  $\mathcal{L}_R$  and  $\mathcal{L}_C$ .** In Eq. 10, the loss function of MiM consists of two parts, namely multi-level reconstruction and cross-level alignment. To determine the suitable class weight for these loss terms, we varied the value of  $\alpha$  in Fig. 8. When we varied the value of  $\alpha$  from a small value of  $1e^{-2}$  to larger

value  $1e^{-1}$  during the pre-training period, it strengthened the impact of cross-level alignment between finer views and larger views, thereby enforcing the representation of local and global alignment. As a result, the DSC of the MiM fine-tuned on the BTCV validation dataset improved by 0.42%. However, further scaling up the weight of cross-level alignment did not bring any additional benefits. This may be because the magnitude of the cross-level alignment function is much larger than the magnitude of the reconstruction loss. Thus, scaling up the weight of cross-level alignment leads the model to ignore the reconstruction process, which is also crucial for MiM method.

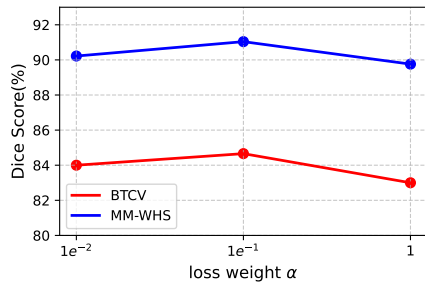


Fig. 8. Evaluation of the loss weight  $\alpha$  for  $\mathcal{L}_C$ . We report the results on BTCV dataset (Landman et al., 2015).

**Weight of different levels of  $\mathcal{L}_R$ .** To determine the appropriate weights of each level for MiM, we applied different weights to determine the priority of the level of masked 3D medical images during the pre-training, as shown in Fig. 1. Specifically, we explored focusing on reconstructing the coarse level of masked images first, then the finer level (2nd row), and reconstructing the finer level first, then the coarse level of masked images (3rd row) by dynamically updating the weight with a cosine scheduler, as presented in Table 14. The results demonstrated that learning from finer to coarser masked images would help learn a more discriminative representation. Furthermore, we explored simultaneously learning the multi-granularity visual clues (4th row), which outperformed the other settings and set as default choice.

Table 14. Evaluation of the model trained with different learning paradigm by varying the weight of each level of  $\mathcal{L}_R$ , respectively. We reprot Disce Score (%) on BTCV (Landman et al., 2015) and MM-WHS (Zhuang, 2018) dataset.

Learning process	Weight			Datasets	
	Level-1	Level-2	Level-3	BTCV	MM-WHS
w/o Coarse & Fine	0→0	0→0	0→0	81.49	89.42
Coarse→Fine	2→1	0→1	0→1	83.99	90.70
Fine→Coarse	1→1	0→1	2→1	84.26	90.85
Simultaneously	1→1	1→1	1→1	84.66	91.04

#### 4.7.3. Reconstruction results

We provided reconstruction results of MiM on BTCV (Landman et al., 2015) in Fig. 9, where the first and second rows represent the volumes and masked 3D medical images, respectively, and the reconstruction results in the last row demonstrate excellent performance.

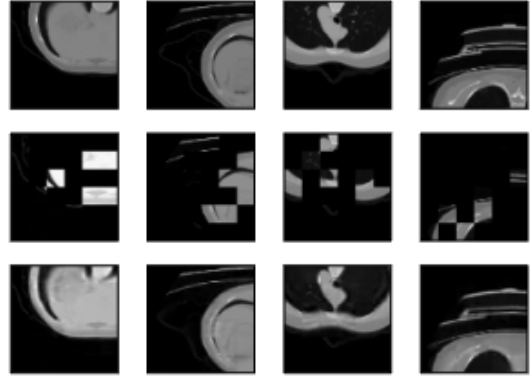


Fig. 9. Reconstruction results of the proposed method MiM on the BTCV validation dataset (Landman et al., 2015).

## 5. Discussion

### 5.1. Limitations

While our MiM framework has shown promising results, our MiM does have limitations. In our experiments, we only scaled up the MiM to a *10k* pre-training dataset, which may not be sufficient to fully explore its potential. Previous works in Natural Language Processing (Kaplan et al., 2020) and Computer Vision (Kaplan et al., 2020; Wang et al., 2023c) have demonstrated that scaling up the pre-training dataset to *billions* of images can lead to the foundation model for their fields (Kaplan et al., 2020), but collecting enough high-quality 3D medical images remains challenging. Therefore, further exploration is needed to investigate the performance of MiM with a vast scale of pre-training datasets, such as *100k*.

Moreover, while the hierarchical design is effective, we adopted a simple design in the experiments to consider computation costs. For the generation of multi-level volumes, we employed a random sampling strategy to select the masked patches as next-level volumes, which achieved good performance. Since not all patches are equally important Li et al. (2021), Wang et al. (2023a) proposed a hard negative mining strategy to sample the patches for reconstruction. Future exploration can design priory sampling strategy *i.e.*, selecting the most informative patches for finer level reconstruction, to further improve the performance of MiM. Finally, as our MiM framework mainly mines the hierarchical structure for intra-volume relationships, it can be extended to explore its capacity in mining inter-volume relationships, which may further improve its performance.

### 5.2. Future directions and challenges

The foundation model has the potential to advance healthcare (He et al., 2024), and SSL is a promising direction for building the foundation model in 3D medical images (He et al., 2024; Achiam et al., 2023). However, there are current limitations that need to be addressed. To build upon the 3D medical image foundation model with SSL, several promising emerging directions can be explored. (1) Building up a large-scale pre-training datasets, *e.g.*, more than 100k volumes. (2) Exploring more downstream tasks, *e.g.*, 3D medical image registration (Zhao et al., 2019), and tumor synthesis (Hu

et al., 2023). (3) Exploring cooperation with other modalities for multi-modal pre-training, *e.g.*, language (Wu et al., 2023a; Achiam et al., 2023; Li et al., 2020). Actually, (1) is the cornerstone for the foundation model in 3D medical images, and (2) can further comprehensively evaluate the performance of SSL for 3D medical image analysis. Since existing SSL methods often pre-train with a limited scale of data and evaluate on limited downstream tasks, which cannot lead to a healthcare foundation model for 3D medical images (Wu et al., 2023a). Inspired by the success of Achiam et al. (2023); Radford et al. (2021), multi-modal pre-training for 3D medical image analysis also deserves more attention, which can learn robust representation by complementing the information from different modalities.

## 6. Conclusion

In this paper, we introduce the Mask in Mask (MiM) pre-training framework, which significantly advances 3D medical image analysis. MiM improves MAE by facilitating the learning of hierarchical visual tokens across various scales. This results in a robust representation for transfer learning in downstream application-specific tasks. By incorporating hierarchical designs, *i.e.*, multi-level reconstruction and cross-level alignment, MiM efficiently encodes multi-granularity visual cues of structure and details into the representation. To facilitate the fair and comprehensive comparison of existing methods, we collected ten public datasets and curated two scales of pre-training datasets, *i.e.*, **1k** and **10k**. Consistent with existing works, we pre-trained our MiM on a **1k** dataset, and extensive experiments on thirteen datasets demonstrate MiM’s effectiveness in achieving superior performance over other methods, including segmentation and classification tasks. We also transferred the learned representation of MiM to MRI-based tasks to evaluate the cross-modality generalization ability. Additionally, we conducted an ablation study to validate the importance of each component of MiM. We conducted a hyper-parameter analysis to investigate the impact of different hyper-parameters on the performance of MiM. The results reveal that the hierarchical design of the MiM framework is crucial for achieving superior performance for 3D medical images. We further explore to scale up the pre-training dataset to **10k**. The results show that the performance of MiM can be further improved by scaling up the pre-training dataset. This finding emphasizes the importance of large-scale pre-training for building the foundation model in 3D medical images. The study hopes to serve as a strong baseline for future research in 3D medical image analysis and draw more attention from the community to the importance of hierarchical design and large-scale pre-training towards the healthcare foundation model.

## 7. Acknowledgments

This work was supported by the Hong Kong Innovation and Technology Fund (Project No. MHP/002/22), Shenzhen Science and Technology Innovation Committee Fund (Project No. SGD20210823103201011), and the Project of Hetao Shenzhen-Hong Kong Science and Technology Innovation Cooperation Zone (HZQB- KCZYB-2020083).

## References

- Achiam, J., Adler, S., Agarwal, S., Ahmad, L., Akkaya, I., Aleman, F.L., Almeida, D., Altschmidt, J., Altman, S., Anadkat, S., et al., 2023. Gpt-4 technical report. arXiv preprint arXiv:2303.08774 .
- An, P., Xu, S., Harmon, S., Turkbey, E.B., Sanford, T.H., Amalou, A., Kassim, M., Varble, N., Blain, M., Anderson, V., et al., 2020. Ct images in covid-19 dataset. The Cancer Imaging Archive 10.
- Armato III, S.G., McLennan, G., Bidaut, L., McNitt-Gray, M.F., Meyer, C.R., Reeves, A.P., Zhao, B., Aberle, D.R., Henschke, C.L., Hoffman, E.A., et al., 2011. The lung image database consortium (lidc) and image database resource initiative (idri): a completed reference database of lung nodules on ct scans. Medical physics 38, 915–931.
- Caron, M., Touvron, H., Misra, I., Jégou, H., Mairal, J., Bojanowski, P., Joulin, A., 2021. Emerging properties in self-supervised vision transformers, in: ICCV, pp. 9650–9660.
- Chaitanya, K., Erdil, E., Karani, N., Konukoglu, E., 2020. Contrastive learning of global and local features for medical image segmentation with limited annotations. NeurIPS 33, 12546–12558.
- Chen, K., Liu, Z., Hong, L., Xu, H., Li, Z., Yeung, D.Y., 2023a. Mixed auto-encoder for self-supervised visual representation learning, in: CVPR, pp. 22742–22751.
- Chen, L., Bentley, P., Mori, K., Misawa, K., Fujiwara, M., Rueckert, D., 2019. Self-supervised learning for medical image analysis using image context restoration. MIA 58, 101539.
- Chen, P., Liu, S., Jia, J., 2021a. Jigsaw clustering for unsupervised visual representation learning, in: CVPR, pp. 11526–11535.
- Chen, R.J., Chen, C., Li, Y., Chen, T.Y., Trister, A.D., Krishnan, R.G., Mahmood, F., 2022. Scaling vision transformers for gigapixel images via hierarchical self-supervised learning, in: CVPR.
- Chen, T., Kornblith, S., Norouzi, M., Hinton, G., 2020a. A simple framework for contrastive learning of visual representations, in: ICML, PMLR. pp. 1597–1607.
- Chen, T., Kornblith, S., Swersky, K., Norouzi, M., Hinton, G., 2020b. Big self-supervised models are strong semi-supervised learners, in: NeurIPS, pp. 22243–22255.
- Chen, X., Fan, H., Girshick, R., He, K., 2020c. Improved baselines with momentum contrastive learning, in: CVPR, pp. 9729–9738.
- Chen, X., Fan, H., Girshick, R., He, K., 2021b. Improved baselines with momentum contrastive learning. CVPR .
- Chen, X., He, K., 2020. Exploring simple siamese representation learning, in: arXiv preprint arXiv:2011.10566.
- Chen, X., Xie, S., He, K., 2021c. An empirical study of training self-supervised vision transformers. in 2021 IEEE, in: ICCV, pp. 9620–9629.
- Chen, Z., Agarwal, D., Aggarwal, K., Safta, W., Balan, M.M., Brown, K., 2023b. Masked image modeling advances 3d medical image analysis, in: WACV, pp. 1970–1980.
- Clark, K., Vendt, B., Smith, K., Freymann, J., Kirby, J., Koppel, P., Moore, S., Phillips, S., Maffitt, D., Pringle, M., et al., 2013. The cancer imaging archive (tcia): maintaining and operating a public information repository. Journal of digital imaging 26, 1045–1057.
- Dosovitskiy, A., Beyer, L., Kolesnikov, A., Weissenborn, D., Zhai, X., Unterthiner, T., Dehghani, M., Minderer, M., Heigold, G., Gelly, S., et al., 2020. An image is worth 16x16 words: Transformers for image recognition at scale. ICLR .
- Dosovitskiy, A., Fischer, P., Springenberg, J.T., Riedmiller, M., Brox, T., 2015. Discriminative unsupervised feature learning with exemplar convolutional neural networks, pp. 1734–1747.
- El-Nouby, A., Klein, M., Zhai, S., Bautista, M.A., Toshev, A., Shankar, V., Susskind, J.M., Joulin, A., 2024. Scalable pre-training of large autoregressive image models. arXiv preprint arXiv:2401.08541 .
- Feng, Z., Zhang, S., 2023. Evolved part masking for self-supervised learning, in: CVPR, pp. 10386–10395.
- Gao, P., Ma, T., Li, H., Lin, Z., Dai, J., Qiao, Y., 2022a. MCMAE: Masked Convolution Meets Masked Autoencoders, in: NeurIPS, pp. 35632–35644.
- Gao, Y., Zhuang, J.X., Lin, S., Cheng, H., Sun, X., Li, K., Shen, C., 2022b. Disco: Remediating self-supervised learning on lightweight models with distilled contrastive learning, in: ECCV, Springer. pp. 237–253.
- Grill, J.B., Strub, F., Altché, F., Tallec, C., Richemond, P., Buchatskaya, E., Doersch, C., Avila Pires, B., Guo, Z., Gheshlaghi Azar, M., et al., 2020. Bootstrap your own latent-a new approach to self-supervised learning. NeurIPS 33, 21271–21284.

- Grossberg, A.J., Mohamed, A.S., Elhalawani, H., Bennett, W.C., Smith, K.E., Nolan, T.S., Williams, B., Chamchod, S., Heukelom, J., Kantor, M.E., et al., 2018. Imaging and clinical data archive for head and neck squamous cell carcinoma patients treated with radiotherapy. *Scientific data* 5, 1–10.
- Haghighi, F., Taher, M.R.H., Gotway, M.B., Liang, J., 2022. Dirac: discriminative, restorative, and adversarial learning for self-supervised medical image analysis, in: *CVPR*, pp. 20824–20834.
- Harmon, S.A., Sanford, T.H., Xu, S., Turkbey, E.B., Roth, H., Xu, Z., Yang, D., Myronenko, A., Anderson, V., Amalou, A., et al., 2020. Artificial intelligence for the detection of covid-19 pneumonia on chest ct using multinational datasets. *Nature communications* 11, 4080.
- Hatamizadeh, A., Nath, V., Tang, Y., Yang, D., Roth, H.R., Xu, D., 2021. Swin unetr: Swin transformers for semantic segmentation of brain tumors in mri images, in: *MICCAI*, Springer. pp. 272–284.
- Hatamizadeh, A., Tang, Y., Nath, V., Yang, D., Myronenko, A., Landman, B., Roth, H.R., Xu, D., 2022. UNETR : Transformers for 3d medical image segmentation, in: *WACV*, pp. 574–584.
- He, K., Chen, X., Xie, S., Li, Y., Dollár, P., Girshick, R., 2022. Masked autoencoders are scalable vision learners, in: *CVPR*, pp. 16000–16009.
- He, K., Fan, H., Wu, Y., Xie, S., Girshick, R., 2020. Momentum contrast for unsupervised visual representation learning, in: *CVPR*, pp. 9729–9738.
- He, K., Zhang, X., Ren, S., Sun, J., 2016. Deep residual learning for image recognition, in: *CVPR*, pp. 770–778.
- He, Y., Huang, F., Jiang, X., Nie, Y., Wang, M., Wang, J., Chen, H., 2024. Foundation model for advancing healthcare: Challenges, opportunities, and future directions. *arXiv preprint arXiv:2404.03264*.
- He, Y., Yang, G., Ge, R., Chen, Y., Coatrieux, J.L., Wang, B., Li, S., 2023. Geometric visual similarity learning in 3d medical image self-supervised pre-training, in: *CVPR*, pp. 9538–9547.
- Hosseinzadeh Taher, M.R., Gotway, M.B., Liang, J., 2023. Towards foundation models learned from anatomy in medical imaging via self-supervision, in: *MICCAI*, Springer. pp. 94–104.
- Hu, Q., Chen, Y., Xiao, J., Sun, S., Chen, J., Yuille, A.L., Zhou, Z., 2023. Label-free liver tumor segmentation, in: *CVPR*, pp. 7422–7432.
- Ji, Y., Bai, H., Ge, C., Yang, J., Zhu, Y., Zhang, R., Li, Z., Zhang, L., Ma, W., Wan, X., et al., 2022. Amos: A large-scale abdominal multi-organ benchmark for versatile medical image segmentation. *NeurIPS* 35, 36722–36732.
- Jiang, Y., Sun, M., Guo, H., Bai, X., Yan, K., Lu, L., Xu, M., 2023. Anatomical invariance modeling and semantic alignment for self-supervised learning in 3d medical image analysis, in: *ICCV*, pp. 15859–15869.
- Jin, C., Guo, Z., Lin, Y., Luo, L., Chen, H., 2023. Label-efficient deep learning in medical image analysis: Challenges and future directions. *arXiv*.
- Kalantidis, Y., Sariyildiz, M.B., Pion, N., Weinzaepfel, P., Larlus, D., 2020. Hard negative mixing for contrastive learning. *NeurIPS* 33, 21798–21809.
- Kaplan, J., McCandlish, S., Henighan, T., Brown, T.B., Chess, B., Child, R., Gray, S., Radford, A., Wu, J., Amodei, D., 2020. Scaling laws for neural language models. *arXiv preprint arXiv:2001.08361*.
- Kingma, D.P., Ba, J., 2014. Adam: A method for stochastic optimization. *arXiv preprint arXiv:1412.6980*.
- Landman, B., Xu, Z., Igelsias, J., Styner, M., Langerak, T., Klein, A., 2015. Miccai multi-atlas labeling beyond the cranial vault—workshop and challenge, in: *MICCAI*, p. 12.
- Li, W., Zhuang, J., Wang, R., Zhang, J., Zheng, W.S., 2020. Fusing metadata and dermoscopy images for skin disease diagnosis, in: *ISBI, IEEE*. pp. 1996–2000.
- Li, Z., Chen, Z., Yang, F., Li, W., Zhu, Y., Zhao, C., Deng, R., Wu, L., Zhao, R., Tang, M., et al., 2021. Mst: Masked self-supervised transformer for visual representation. *Advances in Neural Information Processing Systems* 34, 13165–13176.
- Liu, J., Huang, X., Zheng, J., Liu, Y., Li, H., 2023a. Mixmae: Mixed and masked autoencoder for efficient pretraining of hierarchical vision transformers, in: *CVPR*, pp. 6252–6261.
- Liu, J., Zhang, Y., Chen, J.N., Xiao, J., Lu, Y., A Landman, B., Yuan, Y., Yuille, A., Tang, Y., Zhou, Z., 2023b. Clip-driven universal model for organ segmentation and tumor detection, in: *ICCV*, pp. 21152–21164.
- Liu, Z., Lin, Y., Cao, Y., Hu, H., Wei, Y., Zhang, Z., Lin, S., Guo, B., 2021. Swin transformer: Hierarchical vision transformer using shifted windows, in: *CVPR*, pp. 10012–10022.
- Lyu, Q., Wang, G., 2022. Conversion between ct and mri images using diffusion and score-matching models. *arXiv preprint arXiv:2209.12104*.
- Ma, J., Zhang, Y., Gu, S., Ge, C., Ma, S., Young, A., Zhu, C., Meng, K., Yang, X., Huang, Z., et al., 2023. Unleashing the strengths of unlabeled data in pan-cancer abdominal organ quantification: the flare22 challenge. *arXiv preprint arXiv:2308.05862*.
- Myronenko, A., 2019. 3d mri brain tumor segmentation using autoencoder regularization, in: *MICCAI*, Springer. pp. 311–320.
- Pathak, D., Krahenbuhl, P., Donahue, J., Darrell, T., Efros, A.A., 2016. Context encoders: Feature learning by inpainting, in: *CVPR*, pp. 2536–2544.
- Radford, A., Kim, J.W., Hallacy, C., Ramesh, A., Goh, G., Agarwal, S., Sastry, G., Askell, A., Mishkin, P., Clark, J., et al., 2021. Learning transferable visual models from natural language supervision, in: *ICML, PMLR*. pp. 8748–8763.
- Revel, M.P., Boussouar, S., de Margerie-Mellon, C., Saab, I., Lapotre, T., Mompont, D., Chassagnon, G., Milon, A., Lederlin, M., Bennani, S., et al., 2021. Study of thoracic ct in covid-19: the stoic project. *Radiology* 301, E361–E370.
- Ronneberger, O., Fischer, P., Brox, T., 2015. U-net: Convolutional networks for biomedical image segmentation, in: *MICCAI*, Springer. pp. 234–241.
- Roth, H.R., Xu, Z., Tor-Díez, C., Jacob, R.S., Zember, J., Molto, J., Li, W., Xu, S., Turkbey, B., Turkbey, E., et al., 2022. Rapid artificial intelligence solutions in a pandemic—the covid-19-20 lung ct lesion segmentation challenge. *MIA* 82, 102605.
- Shen, D., Wu, G., Suk, H.I., 2017. Deep learning in medical image analysis. *Annual review of biomedical engineering* 19, 221–248.
- Simpson, A.L., Antonelli, M., Bakas, S., Bilello, M., Farahani, K., Van Ginneken, B., Kopp-Schneider, A., Landman, B.A., Litjens, G., Menze, B., et al., 2019. A large annotated medical image dataset for the development and evaluation of segmentation algorithms. *arXiv*.
- Singh, M., Duval, Q., Alwala, K.V., Fan, H., Aggarwal, V., Adcock, A., Joulin, A., Dollár, P., Feichtenhofer, C., Girshick, R., et al., 2023. The effectiveness of mae pre-training for billion-scale pretraining. *arXiv preprint arXiv:2303.13496*.
- Tajbakhsh, N., Jeyaseelan, L., Li, Q., Chiang, J.N., Wu, Z., Ding, X., 2020. Embracing imperfect datasets: A review of deep learning solutions for medical image segmentation. *MIA* 63, 101693.
- Taleb, A., Loetzsch, W., Danz, N., Severin, J., Gaertner, T., Bergner, B., Lippert, C., 2020. 3d self-supervised methods for medical imaging. *NeurIPS* 33, 18158–18172.
- Tang, Y., Yang, D., Li, W., Roth, H.R., Landman, B., Xu, D., Nath, V., Hatamizadeh, A., 2022. Self-supervised pre-training of swin transformers for 3d medical image analysis, in: *CVPR*, pp. 20730–20740.
- Tao, X., Li, Y., Zhou, W., Ma, K., Zheng, Y., 2020. Revisiting rubik’s cube: self-supervised learning with volume-wise transformation for 3d medical image segmentation, in: *MICCAI*, Springer. pp. 238–248.
- Tong, Z., Song, Y., Wang, J., Wang, L., 2022. Videomae: Masked autoencoders are data-efficient learners for self-supervised video pre-training. *NeurIPS* 35, 10078–10093.
- Vincent, P., Larochelle, H., Lajoie, I., Bengio, Y., Manzagol, P.A., Bottou, L., 2010. Stacked denoising autoencoders: Learning useful representations in a deep network with a local denoising criterion. *Journal of machine learning research* 11.
- Wang, H., Song, K., Fan, J., Wang, Y., Xie, J., Zhang, Z., 2023a. Hard patches mining for masked image modeling, in: *CVPR*, pp. 10375–10385.
- Wang, H., Tang, Y., Wang, Y., Guo, J., Deng, Z.H., Han, K., 2023b. Masked image modeling with local multi-scale reconstruction, in: *CVPR*, pp. 2122–2131.
- Wang, L., Huang, B., Zhao, Z., Tong, Z., He, Y., Wang, Y., Wang, Y., Qiao, Y., 2023c. Videomae v2: Scaling video masked autoencoders with dual masking, in: *CVPR*, pp. 14549–14560.
- Wang, W., Wang, J., Chen, C., Jiao, J., Cai, Y., Song, S., Li, J., 2024. Fremim: Fourier transform meets masked image modeling for medical image segmentation, in: *WACV*, pp. 7860–7870.
- Wang, Y., Li, Z., Mei, J., Wei, Z., Liu, L., Wang, C., Sang, S., Yuille, A.L., Xie, C., Zhou, Y., 2023d. Swinmm: masked multi-view with swin transformers for 3d medical image segmentation, in: *MICCAI*, Springer. pp. 486–496.
- Wasserthal, J., Meyer, M., Breit, H.C., Cyriac, J., Yang, S., Segeroth, M., 2022. Totalsegmentator: robust segmentation of 104 anatomical structures in ct images. *Radiology: Artificial Intelligence*.
- Wolf, D., Payer, T., Lisson, C.S., Lisson, C.G., Beer, M., Götz, M., Ropinski, T., 2023. Self-supervised pre-training with contrastive and masked autoencoder methods for dealing with small datasets in deep learning for medical imaging. *Scientific Reports* 13, 20260.
- Wu, C., Zhang, X., Zhang, Y., Wang, Y., Xie, W., 2023a. Towards generalist foundation model for radiology. *arXiv preprint arXiv:2308.02463*.



- Wu, L., Fang, L., He, X., He, M., Ma, J., Zhong, Z., 2023b. Querying labeled for unlabeled: Cross-image semantic consistency guided semi-supervised semantic segmentation. *IEEE T-PAMI* .
- Wu, L., Zhuang, J., Chen, H., 2024. Voco: A simple-yet-effective volume contrastive learning framework for 3d medical image analysis, in: *arXiv*.
- Xiao, J., Bai, Y., Yuille, A., Zhou, Z., 2023. Delving into masked autoencoders for multi-label thorax disease classification, in: *WACV*, pp. 3588–3600.
- Xie, Y., Zhang, J., Liao, Z., Xia, Y., Shen, C., 2020. Pgl: prior-guided local self-supervised learning for 3d medical image segmentation. *arXiv* .
- Xie, Y., Zhang, J., Xia, Y., Wu, Q., 2022a. Unimiss: Universal medical self-supervised learning via breaking dimensionality barrier, in: *ECCV*, Springer. pp. 558–575.
- Xie, Z., Zhang, Z., Cao, Y., Lin, Y., Bao, J., Yao, Z., Dai, Q., Hu, H., 2022b. SimMIM: A simple framework for masked image modeling, in: *CVPR*, pp. 9653–9663.
- Ye, Y., Zhang, J., Chen, Z., Xia, Y., 2022. Desd: Self-supervised learning with deep self-distillation for 3d medical image segmentation, in: *MICCAI*, Springer. pp. 545–555.
- Zhang, C., Zheng, H., Gu, Y., 2023. Dive into the details of self-supervised learning for medical image analysis. *MIA* 89, 102879.
- Zhang, K., Liu, X., Shen, J., Li, Z., Sang, Y., Wu, X., Zha, Y., Liang, W., Wang, C., Wang, K., et al., 2020. Clinically applicable ai system for accurate diagnosis, quantitative measurements, and prognosis of covid-19 pneumonia using computed tomography. *Cell* 181, 1423–1433.
- Zhang, R., Guo, Z., Gao, P., Fang, R., Zhao, B., Wang, D., Qiao, Y., Li, H., 2022a. Point-m2ae: multi-scale masked autoencoders for hierarchical point cloud pre-training. *NeurIPS* 35, 27061–27074.
- Zhang, T., Qiu, C., Ke, W., Süssstrunk, S., Salzmann, M., 2022b. Leverage your local and global representations: A new self-supervised learning strategy, in: *CVPR*, pp. 16580–16589.
- Zhang, Z., Gong, X., 2023. Positional label for self-supervised vision transformer, in: *AAAI*, pp. 3516–3524.
- Zhao, S., Lau, T., Luo, J., Eric, L., Chang, C., Xu, Y., 2019. Unsupervised 3d end-to-end medical image registration with volume tweening network. *JBHI* 24, 1394–1404.
- Zhao, Z., Yang, G., 2021. Unsupervised contrastive learning of radiomics and deep features for label-efficient tumor classification, in: *MICCAI*, Springer. pp. 252–261.
- Zhou, H.Y., Guo, J., Zhang, Y., Yu, L., Wang, L., Yu, Y., 2021a. nnformer: Interleaved transformer for volumetric segmentation. *arXiv* .
- Zhou, H.Y., Lu, C., Chen, C., Yang, S., Yu, Y., 2023. A unified visual information preservation framework for self-supervised pre-training in medical image analysis. *IEEE T-PAMI* .
- Zhou, H.Y., Lu, C., Yang, S., Han, X., Yu, Y., 2021b. Preservation learning improves self-supervised medical image models by reconstructing diverse contexts, in: *ICCV*, pp. 3499–3509.
- Zhou, Z., Sodha, V., Pang, J., Gotway, M.B., Liang, J., 2021c. Models genesis. *MIA* 67, 101840.
- Zhu, J., Li, Y., Hu, Y., Ma, K., Zhou, S.K., Zheng, Y., 2020. Rubik’s cube+: A self-supervised feature learning framework for 3d medical image analysis. *MIA* 64, 101746.
- Zhuang, J.X., Cai, J., Zhang, J., Zheng, W.s., Wang, R., 2023a. Class attention to regions of lesion for imbalanced medical image recognition. *Neurocomputing* 555, 126577.
- Zhuang, J.X., Luo, L., Chen, H., 2023b. Advancing volumetric medical image segmentation via global-local masked autoencoder. *arXiv* .
- Zhuang, X., 2018. Multivariate mixture model for myocardial segmentation combining multi-source images. *IEEE T-PAMI* 41, 2933–2946.